UNIVERSITY OF CALIFORNIA SAN DIEGO

Moisture Ingress and Distribution in Bifacial Silicon Photovoltaics

A Thesis submitted in partial satisfaction of the
requirements for the degree Master of Science

in

NanoEngineering

by

Tala Sidawi

Committee in charge:

Professor David Fenning, Chair
Professor Jan Kleissl
Professor Oscar Vazquez Mena

2022

The Thesis of Tala Sidawi is approved, and it is acceptable in quality and form for publication on microfilm and electronically.

University of California San Diego

2022

EPIGRAPH

Be kind.

Dr. Rishi Eugene Kumar

TABLE OF CONTENTS

LIST OF FIGURES

LIST OF TABLES

ACKNOWLEDGEMENTS

I would like to express my gratitude and appreciation to Professor David Fenning whose guidance has been invaluable these past two years. Thank you for encouraging me to step out of my comfort zone and helping me succeed in research that I'm extremely proud of. I'm also extremely grateful to Rishi Kumar, whose leadership and collaboration have shaped me into the skilled scientist I am today. I can confidently say that I have learned more from you in these past two years than I have in my entire life. Thank you for being a trusted friend, an intelligent colleague, and an incredibly inspiring mentor to me throughout my time at UCSD.

I also had the pleasure of working with and getting to know everyone from SOLEIL. Thank you Connor, Isabel, Robert, Jack, and everyone else for always encouraging insightful discussions, teaching me Python, and innovating solar energy with me.

Thank you to all of my dear friends, both in California and Georgia, for supporting me in achieving my goals and always being ready to celebrate my successes. Many thanks to Mom, Dad, Noor, Sean, Sugar, Sarah, Cheyenne, Loren, Josh, Sebastiaan, and the entire 2021 MS1 class. You all have made San Diego a home away from home, and I thank you all deeply for that. I would like to extend a special congratulations to Karim Sidaoui, who received his doctorate while helping me get through my masters.

Chapters 1-4, in full, are currently being prepared for submission for publication of the material. Sidawi, Tala; Kumar, Rishi E.; Slauch, Ian; Meier, Rico; Bertoni, Mariana I.; Fenning, David P. The thesis author was the primary investigator and author of this material.

ABSTRACT OF THE THESIS

Moisture Ingress and Distribution in Bifacial Silicon Photovoltaics

by

Tala Sidawi

Master of Science in NanoEngineering

University of California San Diego, 2022

Professor David Fenning, Chair

Water accelerates various modes of degradation in silicon photovoltaic (PV) modules including encapsulant yellowing, delamination, and contact corrosion. Moisture primarily enters silicon PV modules through the polymeric module components (encapsulant and backsheet). To mitigate moisture-induced degradation, we must understand the dynamics of moisture in state-of-the-art encapsulants and module architectures. In this work, we present a robust optical method to quantify water content on the front and rear side encapsulants in bifacial silicon PV modules and use such measurements to validate a model for simulating water concentration in these modules. First, we quantify the solubility and diffusivity of water in four modern encapsulants: ethylene vinyl acetate (EVA) and polyolefin (POE) both with and without UV-blocking additives.

Second, we measure water concentration within glass-glass and glass-backsheet using water reflectometry detection (WaRD), tracking the diffusion of moisture throughout the modules as a function of time and environmental condition. Crucially we separate the water content from the front encapsulant and rear encapsulant and backsheet within the glass-backsheet modules. Third, we present a model of moisture dynamics in bifacial silicon PV modules and show it to be consistent with our measurements. Finally, we apply this model to simulate the concentration profile of water typical fielded climates as a function of time, environmental conditions, cell size, and module architecture. Overall, our work presents: 1) a quantitative picture of water dynamics in industrially relevant module architectures and field conditions, and 2) a framework to extend this approach to other encapsulants and module designs.

Chapter 1

Introduction

1.1 Global Energy Demand and Renewable Energy

Given the rapid increase in the global population over the past century, we are at a time in history where the potential for an energy crisis amplifies with each year. The primary energy consumption of the world has steadily increased almost every year since 1966, but country-specific data shows that, recently, this upwards trend is due to the population growth of developing countries [1]. The pressure for widespread, accessible energy is increasing as high energy demand in these countries parallels economic growth [2]. This necessary resource, combined with the impending danger of climate change, introduces an obligation for the future of our energy consumption and survival capabilities. It is therefore critical to consider renewable energy sources as a viable alternative for non-renewable fossil fuels, especially as the prices of oil, natural gas, and coal have been trending upward, indicating that global supply is unable to meet the rising energy demand [3]. Fortunately, the price of renewable energy has optimistically decreased. In the case of solar energy, utility-scale photovoltaic (PV) systems have reduced in cost by 82% over the last decade (Figure 1.1), reaching grid parity in China, California, and some European countries [4, 5]. Technological breakthroughs, larger scale applications, and cheaper material costs continue to advance this goal of producing affordable solar electricity.

Since its first iteration, the basic research challenges for solar as a resource can be categorized by innovation in improving cell efficiency, manufacturing costs, and module reliability [6].

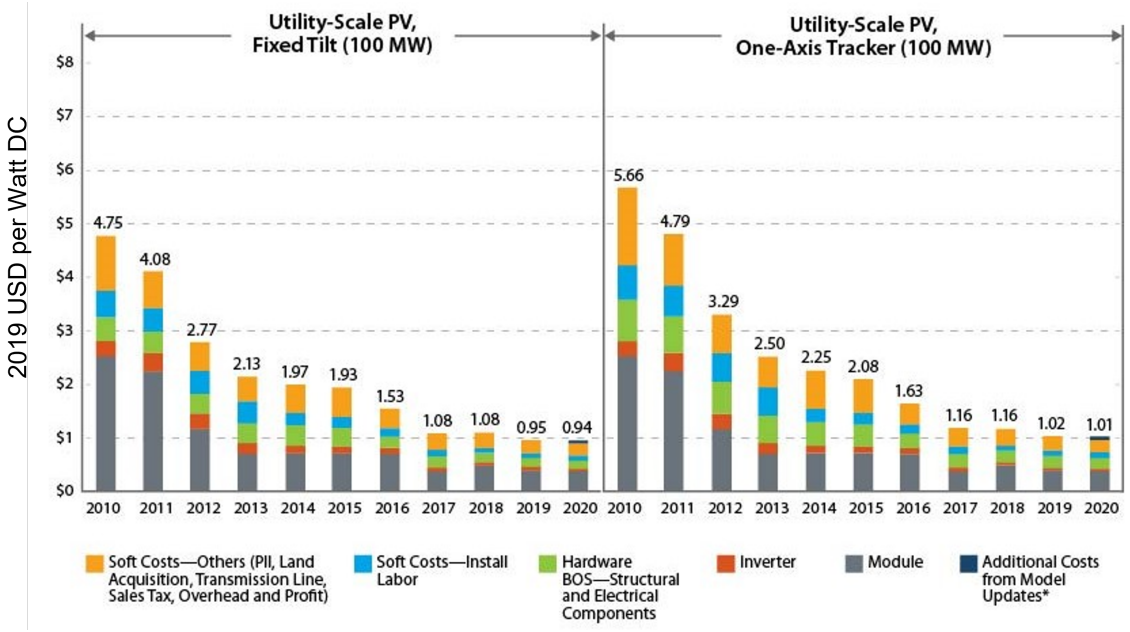

Figure 1.1. Inflation adjusted cost benchmark summary of utility scale solar from 2010-2020 [4].

Higher efficiency cells directly reduce costs by improving power density output (electrical energy output per unit area over the operational lifetime of the module). Additionally, the historical cost of solar follows a ”80% learning curve,” which describes how the price of PV has dropped by 20% globally every time the total number of PV modules has doubled [7]. Using this price reduction trend, we are predicted to reach a module price of $1/watt when the cumulative world production of solar reaches 75,000 MW. According to the 2021 BP Statistical Review of World Energy, the global generation of electricity from solar reached 1023.1 TWh [3]. Figure 1.1 shows that the current cost of utility scale PV has dropped even below $1/watt, and this price will continue to follow the learning curve trend and decrease as the solar industry continues to grow.

1.2 Silicon Photovoltaics

1.2.1 Module Architectures

The three general physical processes that lead to photovoltaic energy conversion in standard silicon devices are 1) excitation of electrons from light absorption at or below 1100

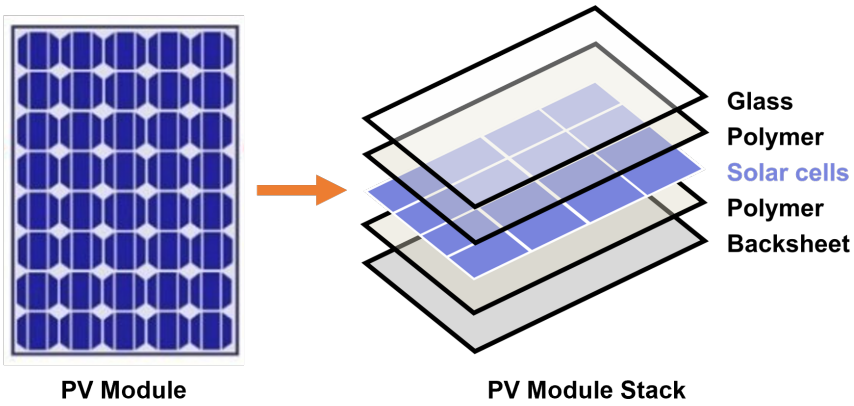

Figure 1.2. Schematic of the components of a glass-backsheet PV module.

nm wavelengths into the conduction band of the material, 2) separation of electrons and holes to reduce carrier relaxation and recombination into the valance band (carrier lifetimes), and 3) collection of excited electrons from the conduction band into metallic contacts to generate a current and power an external load. To protect solar cells and ensure reliability of the operational lifetime, cells are assembled within stack of glass, polymer adhesives, and a layer of impermeable (glass) or permeable (backsheet) material on the backside (Figure 1.2). Glass-glass (GG) packaged modules use an edge-seal to reduce damage from penetrative particulates or water vapor. Alternatively, glass-backsheet (GBS) architectures omit the extra glass layer on the backside and are advertised as ”breathable”, reducing transportation and manufacturing costs at the risk of increased moisture into the module. However, the higher rate of ingress into the module is accompanied by a higher rate of egress out of the polymer, reducing the potential for moisture and acetic acid pooling and additional catalytic degradation [8]. Arihara et al. compared the reliability of GG and GBS bifacial cell modules in damp heat environments with the same polymeric encapsulant on both sides of the cell [9]. They tested the UV exposure with an irradiation of 3 sun at 300-400 nm for 3000h to simulate an installation in Arizona for 50 years. They reported that the transparent backsheet degradation due to UV and damp heat exposure was minimal, suggesting that the PET transparent backsheet is resilient to moisture and UV degradation.

1.2.2 Bifacial Silicon Photovoltaics

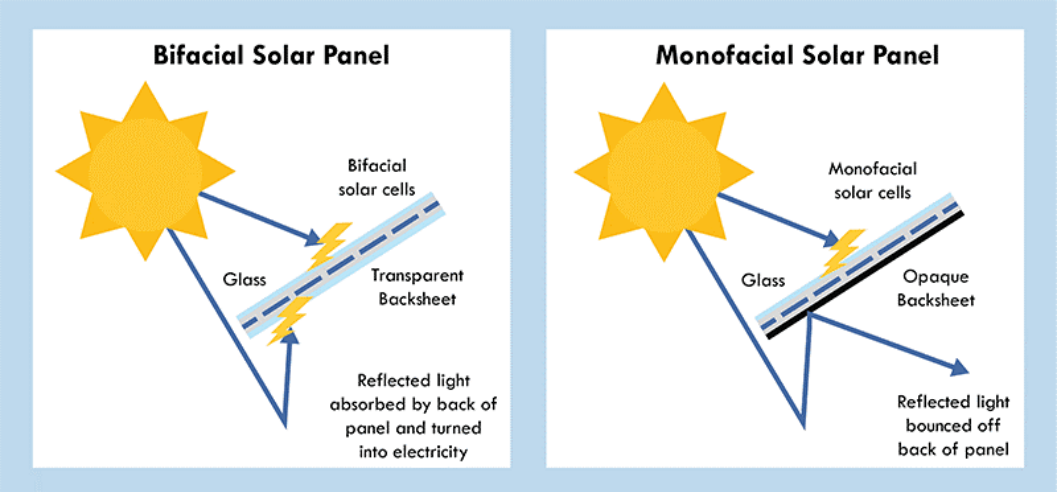

Figure 1.3. Advantages of a bifacial solar panel array compared to a monofacial solar panel [10]

Monofacial or one-sided solar panels are designed to optimize internal reflections within the module, where incident light rays that are not immediately absorbed by the silicon bulk have a second chance of exciting an electron if the ray can reflect back into the module [11]. An opaque rear cover on the backside, seen in Figure 1.3, reflects incident light on the backside away from the module, but encourages light trapping within the bulk, increasing the probability of carrier generation. Bifacial PV modules reduce the levelized cost of electricity by using incident light from the albedo to produce 50% more power under specific testing conditions, with a significant advantage in absorbing diffuse light on cloudy days [12]. Bifacial passivated emitter rear cells (PERC) use an Al finger grid design on the backside of the cell, increasing the passivation surface area for silicon, reducing surface recombination and improving performance [13]. In the absence of a full-area aluminum back contact, less infrared ($\lambda > 1200$ nm) light is absorbed and the working temperature of the module is decreased, also increasing maximum power output [14].

To reduce solar costs, bifacial cells can generate more power using the same area already reserved for solar farm installations. The improvement of energy conversion efficiencies increases power density, overall reducing area-related costs which account for 70% of costs for a traditional

PV system [15]. In addition to power density improvements, transparent backsheets (compared to white backsheets) for packaging bifacial cell modules (Figure 1.3) are used to take advantage of reflected and diffuse light on the backside [16]. These lighter weight, double-sided modules can be manufactured using the a similar process as monofacial GBS modules but face the issue of UV degradation from reflected light on the backside of the cell through the transparent PET backsheet [9]. This can be answered by adding UV-blocking properties to the polymer encapsulant layers on the backside that are optically opaque at λ longer than 360 nm [17],[18], [19].

1.3 Degrading Effects of Water and Heat on the Operational Lifetime of Solar Cells

The operational lifetime of current crystalline silicon is about 30 years, with a manufacturer guarantee that the power generation will not decrease by more than 20% for the first 25 years [20]. As modern day commercial PV installations reach their service lifetimes, the effects of climate-induced degradation modes are becoming increasingly apparent. Gradual losses in performance negatively impact the total cost of solar by reducing durability, leading to device failure and expensive maintenance or full replacements. Causes of PV performance degradation during deployment can be categorized into four main factors [21]:

- Temperature
- Irradiation
- Humidity
- Mechanical Stress

Some various defects as a result of prolonged exposure to these stresses are listed in Figure 1.4, showing the wide range of reported failure modes. Noticeably, a majority of PV modules suffer performance losses from discoloration (yellowing) [23], [24] and delamination (damaging of the interfacial bonds of the polymer layer, creating air bubbles) [21], [25], [26] of the polymeric

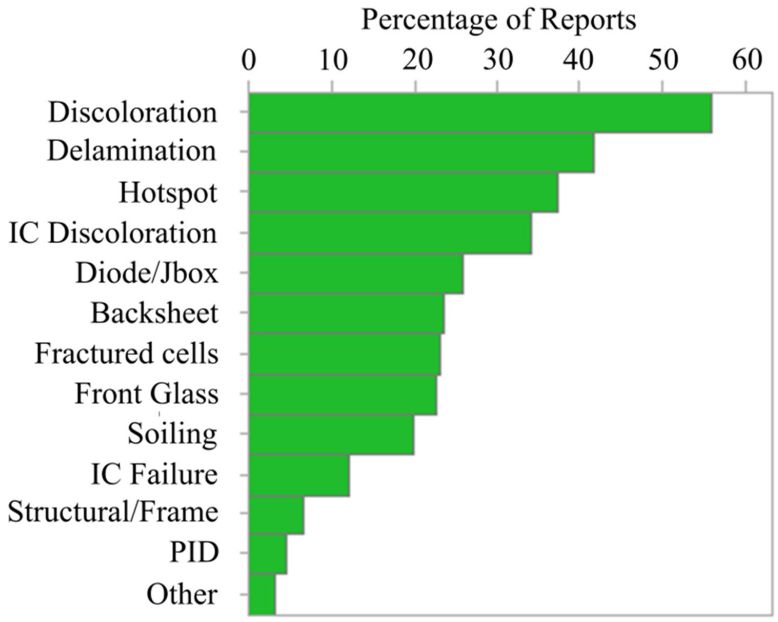

Figure 1.4. Percentage of various degradation modes reported in literature [22].

encapsulant that has good adhesion to the glass layer, high transmittance, and protects the cell from UV radiation [27], [28]. The industry standard encapsulant used for existing systems is ethylene vinyl acetate co-polymer (EVA), and is sensitive to photodegradation, moisture absorption, and temperatures above 50° C [29], [30]. When exposed to sunlight and heat, photoproducts interact with the vinyl acetate group via the Norrish II reaction (deacetylation) to form acetic acid that can then diffuse through the polymer bulk to the silicon cell layer. At the same time, water vapor enters at the edges of the polymer layer and also diffuses into the into the cell. Moisture in the cell acts as an electrolyte, initiating and sustaining degradation reactions in the presence of carboxylic acids, resulting in corrosion of the silver (Ag) metallization (fingers) and tin (Sb) solder joints, increasing series resistance in the module (Figure 1.5) [31–34]. The issue of moisture degradation was approached via the type of polymer encapsulant used: standard EVA vs polyolefin (POE) encapsulants. Compared to the acetic acid production capabilities of EVA, POE encapsulants consist of long, nonpolar hydrocarbon chains where water can freely move. However, polyolefins are more expensive and allow for faster diffusion times because of fewer C-H and H_2O interactions. - cite bosco et al, fickian diffusion

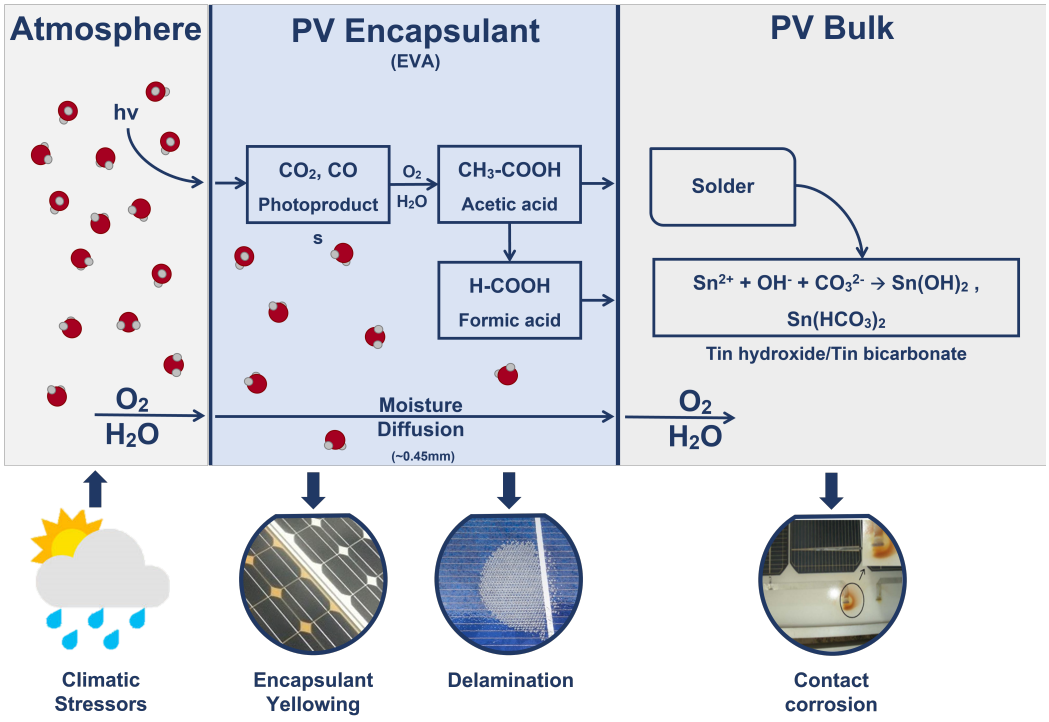

Figure 1.5. Degradation modes and chemical reactions within the polymeric encapsulant and silicon cell caused by climatic stressors, adapted from [35]

Damaging effects are further amplified by the unique intensities of degradation based on geographical location (e.g. a module in Singapore would be exposed to a higher humidity climate than a module in Saudi Arabia). Extended exposure to humid environments can lead to condensation events and water that accumulates in the module during peak heat and humidity seasons. When humid days are followed by cold nights, the condensation of interstitial water vapor in the polymer matrix causes visible cloudiness, as seen in Figure 1.6, where the scattering of incident light limits photon flux in and carrier generation within the module, reducing overall performance. Realistically, there is a need to extend solar operational lifetimes in areas with climates prone to humidity-dependent power losses over the standard 25-year lifetime more than areas with high-year-round irradiance with few to no high humidity seasons. Instead of waiting an additional quarter-century to analyze these effects, we can use accelerated testing to expose lab-scale devices to a similar amount of heat and water over 1000 hours according to the IEC 61215 Photovoltaic Solar Testing Specifications and predict the total energy production of solar

panel arrays well before investment and installation [36]. While this is not perfect, as real-time degradation involves all stress factors at once, the qualification standards are refined enough such that the potential lifetime of a module can be extrapolated.

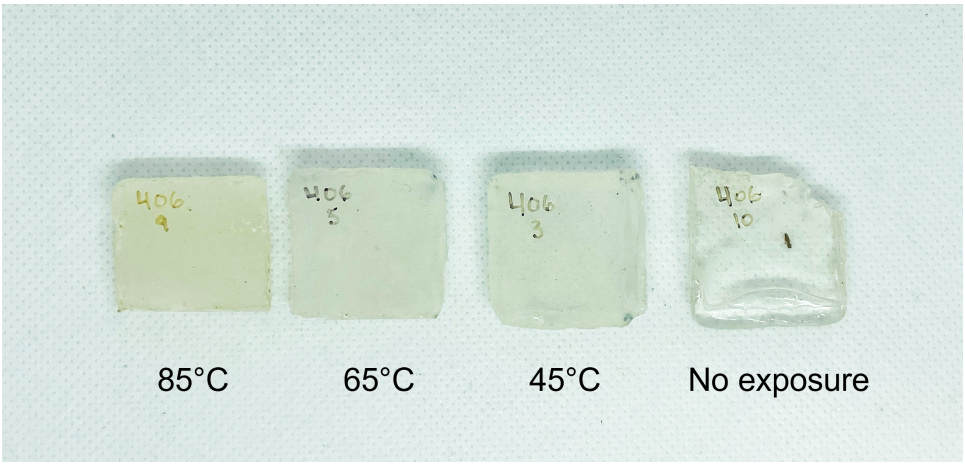

Figure 1.6. Condensation of plain EVA polymer blocks after saturation in varying temperature heated water baths. All polymers were left to cool for 30 min.

1.4 Non-invasive Optical Quantification of Water

Literature in this field has attempted the determination of water ingress rate, local water concentrations, and degradation signal using FTIR and Raman spectroscopy techniques [37–39]. This is because liquid water has a spectroscopic signature (vibrations) in the short wave infrared region (SWIR) with distinct overtones at 1450 and 1900 nm [40]. When measuring water within the EVA polymer matrix, distinct combination bands for interstitial water are apparent at 1902 nm as measured on a monofacial PERC cell, where the glass, cell, and encapsulant are mostly transmissive [41],[42]. In the region of interest (1700 - 2000 nm), the 1730 nm peak is representative of the ethylene C-H stretching overtone [43]. These peaks are labeled in Figure 1.7a. Since the 1730 and 1902 nm peaks do not significantly change with temperature, they can be used to derive the water concentration (Figure 1.7b). This method of water isolation is called water reflectometry detection (WaRD), where the ratio of the baseline-subtracted absorbance of the water absorption feature (A_{H2O}) to the encapsulant absorption feature (A_{EVA})

yields a proportional water concentration from the optical signal that can be calibrated to the true solubility of the polymer.

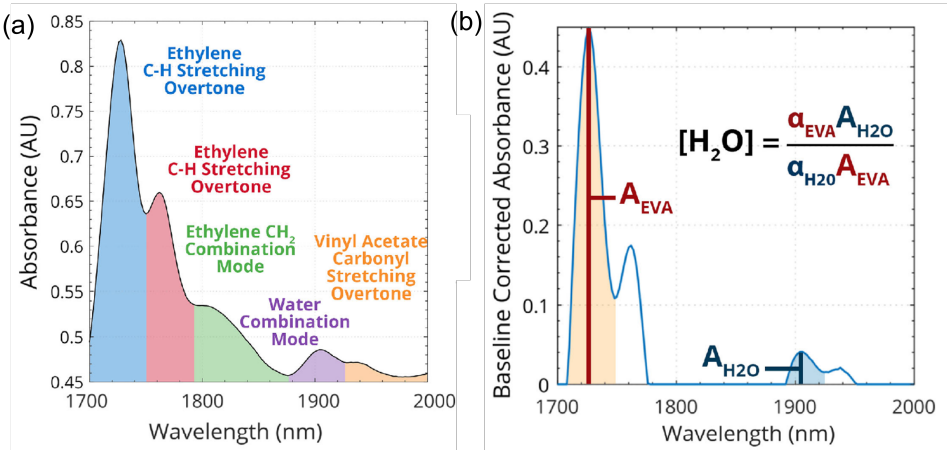

Figure 1.7. SWIR absorbance and WaRD ratio: a) Absorption features of the O-H combination mode of water and the C-H stretching overtone of EVA in the SWIR region, as measured on a monofacial PERC cell b) the baseline subtracted absorption spectrum on the same cell, isolating the water peak of interest with the equation for the calculation of the water concentration [42]

1.5 Scope of Work

This thesis aims to investigate the advantages of bifacial PERC modules packaged with "breathable" materials compared to "non-breathable" double-glass architectures where the encapsulant water diffusion behavior differs and can be predicted with Fickian laws. In glass/glass modules, the water enters laterally on both the front and backsides of the module. In glass/transparent backsheet modules, the permeable transparent backsheet accelerates moisture ingress and facilitates the egress of produced acetic acid out of the module [44]. Acetic acid trapped within a non-permeable module (glass-glass) will reduce the pH of the encapsulant significantly compared to a breathable module due to pooling [31]. The modules in this study will have two types of polymers per module: 1) a plain polymer between the top-side glass and the cell and 2) the same polymer with a UV blocking additive between the cell and the bottom-side layer (glass for GG modules, transparent backsheet for GBS modules). The goal of this study is to understand the behavior of water by measuring the movement of water using WaRD in real

time during accelerated testing for operational lifetime degradation analysis. We use optical characterization methods and simulations to investigate durability with accelerated reliability testing to match and exceed the 25 year operational lifetime in high moisture, solar-viable climates.

Chapter 2

Experimental Methods

2.1 Sample Preparation

2.1.1 Polymer Blocks for Solubility Tests

Multiple layers of industrially relevant polymer were laminated between sheets of Teflon to form 5x5x1 cm and 2x2x0.5 cm standalone blocks of polymer. Repeated for four polymers: polyolefin with (TF8) and without (TF4) ultraviolet-blocking additives, and ethylene vinyl acetate (EVA) with (806) and without (406) ultraviolet-blocking additives.

2.1.2 Mini Modules for Calibration and Diffusivity

Diffusivity tests are performed on either 2.5 cm x 2.5 cm or 6.5" x 6.5" mini-modules made with bifacial p-type PERC silicon cells. Four module architectures are tested: glass-glass and glass-backsheet configurations with either EVA or POE encapsulants. In all cases, the front encapsulant did not have UV-blocking additives, whereas the back encapsulant did; this matches the configuration of fielded modules. All glass sheets are 2 mm float glass, and the backsheet is a transparent Tedlar layer laminated to PET core. Modules are laminated at 150° C for 13 or 15 minutes for EVA or POE, respectively, after a 4.5-minute vacuum step. No edge seals were used.

2.1.3 Modules for Water Mapping and Model Validation

6” c-Si bifacial cells were laminated using a NPC model LM-110x160-S laminator. Those laminates consisted of a Borosilicate glass (8” x 8” x 2mm)/EVA (UV-pass)/cell/EVA (UV-cut)/backsheet stack with the same materials as the mini modules. The cells had 9 busbars and were from JA Solar, soldered with round 250 μm diameter tabbing in a half-cell configuration. Same lamination and vacuum steps as the mini modules.

2.2 Measuring Water Solubility in EVA and POE Encapsulants

2.2.1 Volume of Polymer Blocks

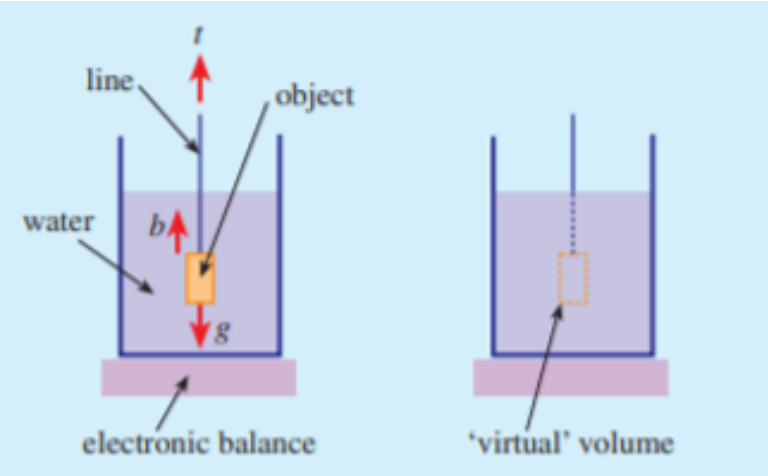

Figure 2.1. Suspension method of measuring volume: Applying buoyancy for a stationary object, the volume of water that the object displaces is equivalent to the ”virtual volume” of water that the liquid was expanded by. Using the measured change in mass and the density of the water, we can solve for the volume of the submerged object. [45].

Because the blocks were irregularly shaped, the volume of each laminated encapsulant block was determined using a revisited Archimedes’ method (Figure 2.1). The available microbalance has a capacity of 215g, which is much lower than the required volume of water needed to measure the 5x5x1 cm POE samples. However, because of the design of the balance, we adapted the revisited Archimedes’ method for our instrument. Using the same application of

buoyancy, the blocks were instead suspended into a beaker of water from a 3D-printed apparatus using fishing line that connected to the arm of the microbalance.

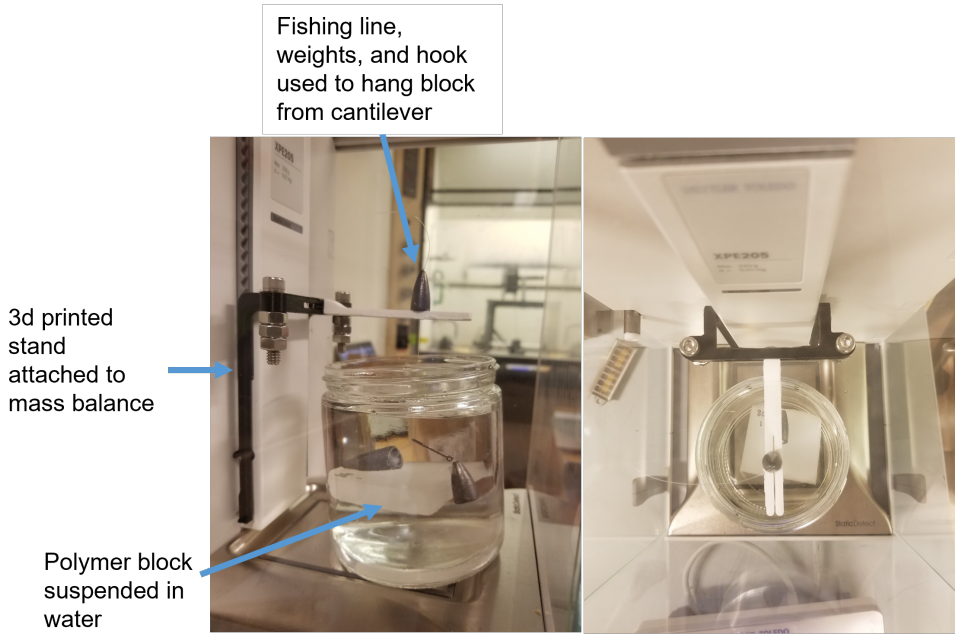

Figure 2.2. Revisited Archimedes' setup, adapted from [45]: The polymer block is attached to a fishing line and weighed down. The weight of the water and the beaker are not measured by the balance in this setup because of the 3D printed stand. The observed decrease in mass of the polymer block represents the mass of the water displaced by the block and provides and accurate measure of the volume of the encapsulant.

A beaker of water was placed underneath the apparatus inside of the microbalance, where the block was completely submerged. Using this setup, the mass of the beaker and water did not affect the sample measurements, allowing for the isolation of the polymer block weight. This way, the force on the balance can be arranged as $F_{balance} = W_{polymer} + F_{buoy_{weights}} - F_{buoy_{polymer}}$ using the free body diagram from Figure 2.1, where $W_{polymer}$ is the initial mass of the polymer (weighed before exposure to solubility tests), $F_{buoy_{weights}}$ is the buoyancy force on the weights when submerged in the water (the balance is zeroed with the weights out of the water), and $F_{buoy_{polymer}}$ is the buoyancy force on the submerged polymer block. Since $F_{buoy_{polymer}} = V_{polymer} \cdot \rho_{water} \cdot g$, we can solve for the volume of the polymer. The mass balance was tared with the apparatus, fishing line, and weights. After submerging the block with the weights, the mass was recorded

over 30 seconds to get the average mass of the block.

2.2.2 Mass Increase from Water Uptake

The masses of the laminated encapsulant blocks were measured using a Mettler XPR Micro-Analytical balance. Three blocks of each encapsulant variant were placed in a heated water bath at temperatures from 35-85° C. Samples stayed in the baths until their masses stabilized, indicating complete water saturation. When saturated, samples were removed from the bath, blasted with clean, dry air for less than 1 minute, and measured on the balance. To calculate the total change in mass, the samples were dried post-hoc (to correct for the acetic acid loss in EVA) and measured after completely drying out. The water solubility was calculated as the change in mass (lost from the saturated to final dry state) divided by the volume.

2.3 Calibration Curve and Measuring the Water Concentration Profile in Modules

2.3.1 Optical Measurement of Water Content

We used Water Reflectometry Detection (WaRD) to measure water content within the modules [42]. A mapping spectrophotometer consisting of a tunable laser (NKT Photonics Compact and Select), translation stage, integrating sphere, and InGaAs detectors was used to spatially resolve module water content in a raster scanning format.

2.3.2 Isolation of Frontside and Backside Signal

We developed a method for isolating the two encapsulants (frontside polymer and backside polymer with backsheet) in the glass-backsheet mini module configuration because of the semitransparency of the bifacial cell (Figure A.1). First, line scans were measured in the NIR region at 1100 nm across the width of the module from the glass-side. These line scans were plotted over the images of the corresponding front and back sides of the module and aligned with the edges of the cell and the fingers. Bifacial silicon cells are semi-transparent in the NIR

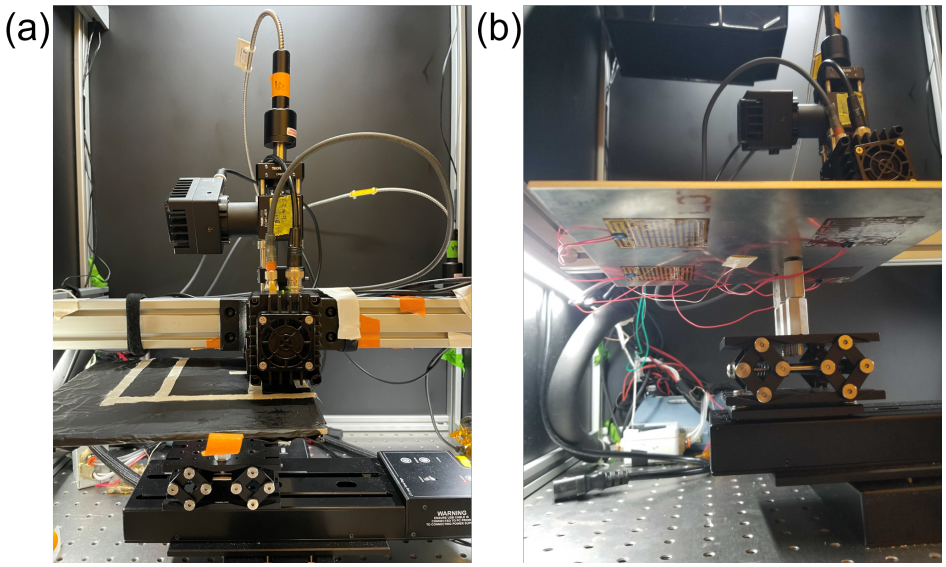

Figure 2.3. WaRD setup with NIR laser: (a) the setup of the movable heated stage under the InGaAs integrating sphere with a reference detector and (b) the heating elements attached to the aluminum stage.

region of interest for water (1700-2000 nm). By scanning at the bandgap of silicon (1100 nm), the cell should be opaque, and the line scan should only contain reflectance information from the fingers on the side of the cell that is measured. Two positions of interest were isolated using this data: frontside finger and backside fingers (measured from the backside) (Figure 2.4a). The physical positions of these points with respect to the cell were extracted from the line scan data for each module. Later, the positional information was used to precisely navigate to the point of interest during the optical measurements for the water concentrations. Four points at different x and y values within the center of the cell were chosen to average any outliers from the calibration measurements.

2.3.3 Generating a Calibration Curve for Polymer Solubility vs WaRD Ratio

The measured WaRD ratio signal was calibrated to the individual polymer water solubility for each type of encapsulant. The expected water concentration (x-axis) was generated from the solubility parameters C_0 and ΔH_{sol} gathered from fitting the Arrhenius relationship

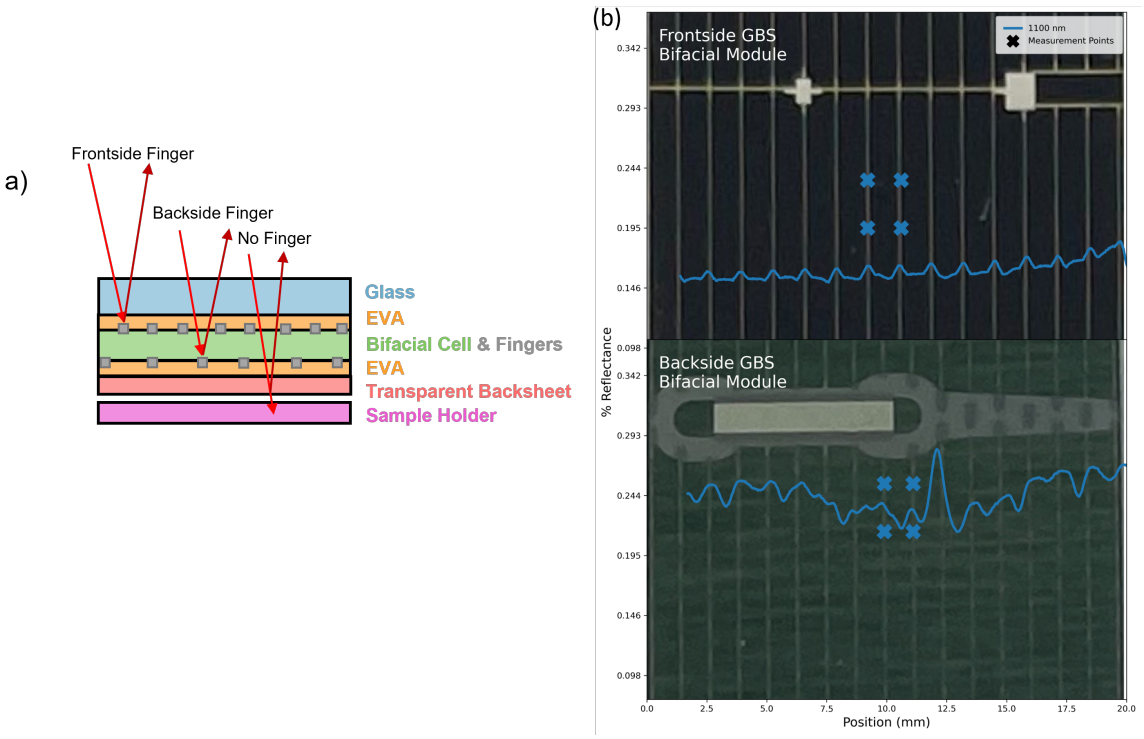

Figure 2.4. Water signal isolation method and plotted absorption of a bifacial module: (a) Schematic of a glass-backsheet bifacial module and optical path of the NIR laser to isolate frontside polymer information from the backside polymer and backsheet. (b) Application of isolation technique on a glass-backsheet EVA bifacial mini module. Line scans at 1100 nm were measured across the width of the module from the frontside and backside and plotted to align with the edge of the cell. Four points for each condition (frontside finger, and backside finger) were identified along the profile of the module using the 1100 nm scan. Linescans at 1700 nm along the module are provided in (Figure B.1)

with an ordinary least squares regression between the water concentration in the polymer and the inverse temperature (1/T). For the optical water signal, bifacial cell mini modules (1x1") with architectures glass/plain polymer/cell/UV-blocking polymer/transparent backsheet and glass/plain polymer/cell/UV-blocking polymer/glass using both EVA and POE polymers were set in damp heat conditions (50-85°C and 45-85% RH) until both sides of polymer were completely saturated. Using the isolation technique, the 1700-2000 nm reflectance was measured for each module at the four locations of interest in each condition, allowing for re-saturation in between measurements.

2.3.4 Diffusivity Measurement During Module Dry Out

Similar to the polymer solubility Arrhenius figure, we calculated the diffusivity as a function of the inverse temperature of these polymers by measuring the rate at which water egressed out of the module over the timescale of days (saturated to room condition equilibrium). Modules with both types of architectures and both types of polymers were used for this experiment. The diffusion pathways for both architecture types are detailed in Figures C.1 and C.2. After the encapsulants were saturated, modules were placed on a heated stage at the same condition temperature to prevent condensation. Full spectrum line scans (1700-2000 nm) were measured along the length of each module with a resolution step size of 2 mm for 3 days of dry out. The WaRD ratio was calculated at each point and the expected water concentration of the polymer was found using the respective calibration curves. Once converted into water signal, the validated model was fit to the experimental data, where the diffusivities of the frontside polymer and backside polymer were predicted. The resultant diffusivities at each temperature were plotted (D vs 1/T) to demonstrate an Arrhenius relationship $D = D_0 e^{\frac{-E_a}{kT}}$. An ordinary least squares regression was fit onto the Arrhenius data to predict parameters for D_0 and E_a for each polymer. This data is not included in this thesis, but is currently in progress at the time of this study.

2.3.5 1D Experimental Water Concentration Profile for Building Model

We built our model using the WaRD signal dry out data of an 8x8" glass–plain EVA–half cut bifacial cell–UV blocking EVA–backsheet (Figure 2.5b) that was exposed to 85°C 85% RH damp heat for ∼6 days. After ∼6 days, the module was measured on a heated stage at 85°C. Similar to the diffusivity measurement data, full spectrum line scans were measured along the short dimension of the half-cut cell (3x6") with a resolution step size of 2 mm for 10 hours. The laser was positioned between the 4th and 5th busbars to capture the dry-out due to the lateral diffusion along the x-dimension with the least amount of influence from the diffusion out of the top of the half-cut cell. We assume that all four quadrants of the module behave the same due to their symmetry, so only one quarter was measured. The WaRD ratio was calculated at each point using the reflectance information and the expected water concentration of the polymer was found using the glass-backsheet EVA calibration curve. The resultant data consisted of a matrix with size 9x41, where each row represents one completed scan along the module that took ∼1.1 hours to complete and each column represents the location of a point along the module.

2.4 Model Validation Using Experimental Data and 2D Simulation of Weather Data

2.4.1 Using FTCS to Predict Water Signal and Diffusivity

Using the measured water profile scans, we built a model for predicting water diffusion in the frontside and backside encapsulants simultaneously. To construct the model, we separated the frontside and backside experimental data by assuming that the backside out-diffusion of water through the backsheet is equal to the change in the midpoint water concentration over the dry-out time. The general diffusion equation,

$$\frac{\partial u}{\partial t} = D_{back}\frac{\partial^2 u}{\partial z^2}, \qquad z \in (0,d), t \in (0,T) \tag{2.1}$$

is applied to the system with the given dimensions for modeling the backside water content and diffusion. The analytical solution to the diffusion equation for the backside dry-out was adapted from [46] as,

$$C_{back}(z,t) = C_{eq,b} - \frac{4(C_{eq,b} - C_{0,b})}{\pi} \sum_{m=0}^{\inf} \frac{1}{2m+1} \sin \frac{(2m+1)\pi(z+d)}{2d} e^{-\frac{D(2m+1)^2\pi^2 t}{(2d)^2}} \tag{2.2}$$

using initial conditions,

$$\begin{gathered} u(z,0) = C_{0,back}, \qquad z \in (0,d) \\ C_{0,back} = [H_2O]_{85C,85\%RH_{EVA806}} \end{gathered} \tag{2.3}$$

with boundary conditions assuming no flux at the cell-encapsulant interface (Neumann) and a fixed concentration on the bottom face of the module (Dirichlet),

$$\begin{gathered} \frac{\partial u}{\partial z}(0,t) = 0, \qquad t \geq 0 \\ u(d,t) = C_{eq,back}, \qquad t \geq 0 \\ C_{eq,back} = [H_2O]_{25C,60\%RH(EVA806)} \end{gathered} \tag{2.4}$$

The predicted backside diffusivity is then used to generate the concentration of water in the backside polymer and backsheet for every time t. The total backside water concentrations are then subtracted from the original set of experimental data to create the frontside-isolated data set. The frontside-isolated water behavior is represented by,

$$\frac{\partial u}{\partial t} = D_{front} \frac{\partial^2 u}{\partial x^2}, \qquad x \in (-m, w+n), t \in (0,T) \tag{2.5}$$

Where the water concentration on the frontside of the module in this experimental data was partially saturated at $t = 0$, thus the initial concentration of water varies across the profile of the

module as a function of position,

$$\begin{aligned} u(x,0) &= f(x), \qquad x \in (0,w) \\ u(x,0) &= u(0,0), \qquad x \in (-m,0) \\ u(x,0) &= u(w,0), \qquad x \in (w,w+n) \end{aligned} \tag{2.6}$$

with Dirichlet boundary conditions,

$$\begin{aligned} u(-m,t) = u(w+n,t) &= C_{eq,front}, \qquad t \geq 0 \\ C_{eq,front} &= [H_2O]_{25C,60\%RH(EVA406)} \end{aligned} \tag{2.7}$$

Because of this, the model for the frontside polymer uses a numerical solution the diffusion equation via the Forward Time Centered Space Finite Difference (FTCS) method (Eq. 2.8) such that we would be able to apply this model to any combination of initial and boundary conditions,

$$u_i^{k+1} = \gamma(u_{i+1}^k - 2u_i^k + u_{i-1}^k) + u_i^k \tag{2.8}$$

where u_i^k is the water concentration at a point in the polymer x and at some time during dry out or saturation t, and u_i^{k+1} is the water concentration at the same space in the polymer x at the next time step $t+1$.

$$\begin{aligned} u(x,t) &= u_i^k \\ u(x,t+1) &= u_i^{k+1} \\ \gamma &= D_{front}\frac{\Delta t}{\Delta x^2} \\ \Delta t &= \frac{1}{2}\frac{\Delta x^2}{D_{front}} \end{aligned} \tag{2.9}$$

Eq. 2.9 includes the stability condition for this method, where for high resolution calculations, the model is constrained to very low time steps. The measured data extends between the edges of the cell as shown in Figure 2.5b from $x \in (0,w)$ with a matrix shape of $[x,t]$. To better match

the real behavior of the module, we padded the edges of the frontside-isolated data (widths m and n on both sides of the module in Figure 2.5b) with the experimental recorded value for the edge concentration of water on both sides (u at $x = 0$ and $x = w$) in EVA 406 for all t ≥ 0. m and n were determined using the measured distances on the module, where m = 1 cm and n = 2.54 cm, and the number of points to be padded was calculated using the step of the mesh size ($\Delta x = 500$ μm). In practice, the actual value for m was 640 μm and n was 640 μm (1 point added on each side). These padded values represent the polymer that extends beyond the area of the bifacial cell to the edge of the glass of the module that exhibits both lateral (2D) diffusion and uniform (1D) diffusion through the backsheet of the module, where the diffusion length is equal to d. Over time, we expect these padded values to out-diffuse water at a faster rate (due to the shorter diffusion length) and reach the equilibrium concentration of water in EVA 406, $C_{eq,front}$. At the edges of the module, we assume that the surrounding air is fixed at a constant temperature and relative humidity (Eq. 2.7). The finite difference approximation for the predicted water concentration at every time step is represented by u_i^{k+1}, where the derivation from the 1D diffusion equation is outlined in [47]. The discretized mesh space $[r,c]$ for the simulation can be represented using $r_i = i\Delta x$ and $c_k = k\Delta t$, where i and k are the discrete points in space and time, respectively, and Δx and Δt describe the grid size. This mesh space is created initially to represent the size of the original data set (over the cell only), where each row of the matrix represents the water concentrations of one completed line scan across the width w of the cell. The initial condition of the experimental data (first row, first completed line scan) is interpolated onto the meshed matrix to set the initial condition of the simulation (Eq. 2.6).

The experimental edge values are padded onto the simulation matrix, where $m * \Delta x$ points are added to the left and $n * \Delta x$ points are added to the right. Lastly, a throwaway value is padded to both sides of the module for all time t to represent the boundary condition of the surrounding air during the measurement (1 point added to each side). The resultant matrix is then iterated at each position for each point in time using the FTCS method (Eq. 2.8). All padded values are then removed to result in a simulated matrix for the original proposed data. Finally, the simulated

matrix is 2D interpolated back to the experimental matrix size $[x,t]$.

The total water signal in the module is described by,

$$C_{WaRD,GB}(x,t) = C_{lateral}(x,t) + r_{GB} \cdot \frac{1}{d} \int_0^d C_{vertical}(z,t)dz \tag{2.10}$$

where $C_{lateral}(x,t)$ is the resultant matrix of simulated concentration values from the FTCS iteration, x is the lateral position in the frontside polymer, z is the vertical position within the bottom half of the module, d is the combined thickness of the bottom encapsulant and backsheet, r is the fraction of reflectance signal from the bottom side of the module (below the cell) as measured from the frontside, and t is time. For GG modules,

$$C_{WaRD,GG}(x,t) = (1 + r_{GG}) \cdot C_{lateral}(x,t) \tag{2.11}$$

describes the frontside lateral diffusion in a GBS module (and both sides of a GG module) and assumes a fixed water concentration at the outer edges of the cell with zero flux across the lateral center of the encapsulant. We used a non-linear least squares regression to predict the parameters of the total water concentration model using d, $C_{0,back}$, and $C_{eq,front}$ as the fixed parameters, and D_{front}, D_{back}, r_{GB}, $C_{eq,back}$ as the variable parameters.

2.4.2 2D Simulation of Real Weather Data

From the validated model, we extended the same theory to a 2-dimensional space [x,y] to simulate the moisture ingress and egress in EVA encapsulants within glass-backsheet architectures. Historical weather data was gathered for Miami, Atlanta, San Diego, and Phoenix for 1 year and 5 year time scales. The water concentration of the module at t = 0 was uniformly initialized at room conditions (25C, 60% RH). Using the same padding technique as the 1D simulation, a ”dummy” border was appended to the matrix and all outer edge points were initialized with the boundary condition at t = 0 for the historical weather data. At every time

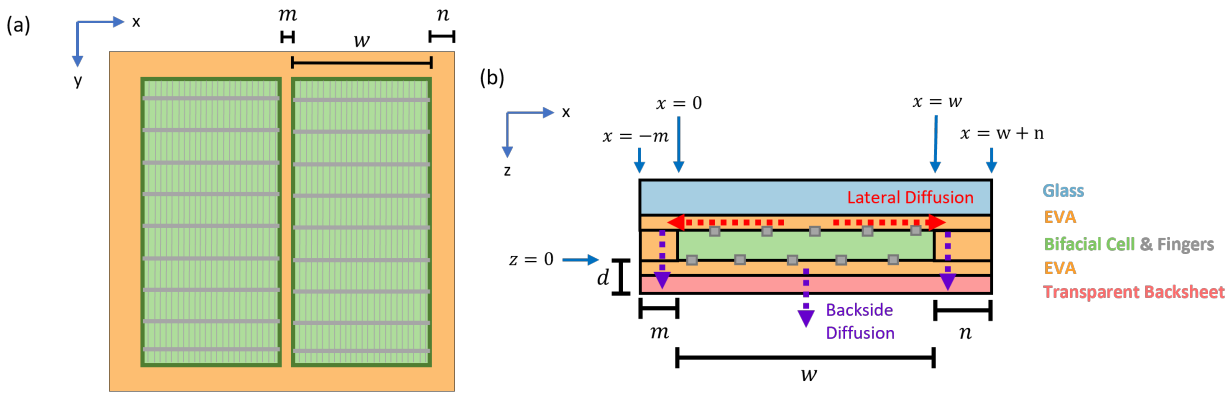

Figure 2.5. FTCS modeling dimensions and diffusion pathways: Schematic of the large GBS bifacial half cut cell module from the (a) topside (glass) and (b) the cross-sectional area of the stack. Critical dimensions for diffusion modeling are shown with black bars. Water pathways are shown for both lateral (frontside) and uniform (backside) diffusion.

point, the values of the boundary conditions are fixed to the equivalent water concentration using the EVA 406 solubility parameters at that time point to represent the Dirichlet boundary conditions at the edges. The polymer diffusivity at every time point is recalculated using the new boundary conditions using the diffusivity of EVA 9100 from [42].

Chapter 3

Results and Discussion

3.1 Solubility and Diffusivity of EVA and POE Polymers

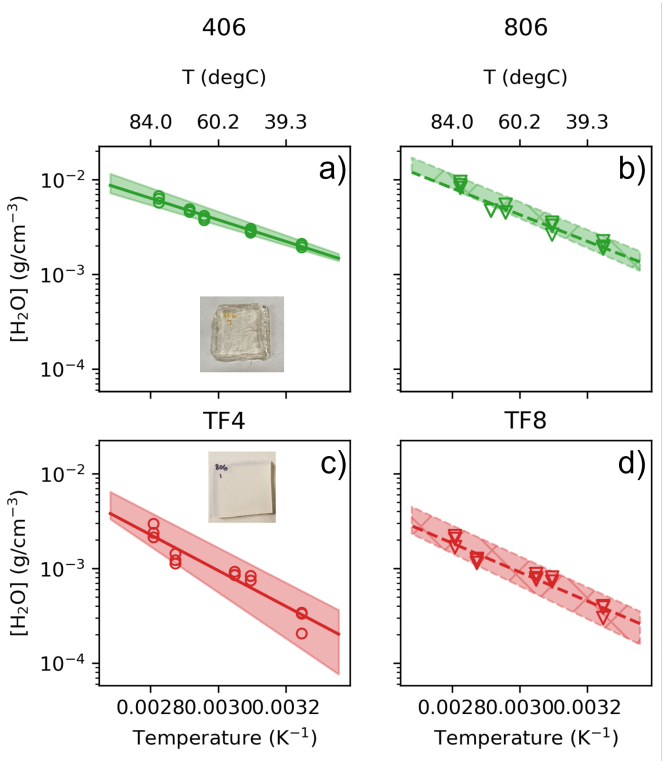

Figure 3.1. Water solubility of EVA and POE encapsulants: Solubility of water in laminated ethylene vinyl acetate (green) and polyolefin (red) encapsulants. Triangles and circles represent encapsulants with and without ultraviolet blocking additives, respectively. The solubility was calculated using gravimetric measurements of saturated sample polymer blocks in heated water baths. The polymer block sample is shown as an inset on a) and c).

We measured the mass of water absorbed by standalone blocks of four module encap-

sulant polymers: polyolefin with (TF8) and without (TF4) UV-blocking agents, and ethylene vinyl acetate with (408) and without (406) UV-blocking agents. This mass uptake, recorded after prolonged soaking in water baths of varied temperature, was used to calculate the saturation concentration of water in each material (Figure 3.1). We extract Arrhenius parameters C_0 and ΔH_{sol} to describe the solubility by fitting the saturation concentrations to the equation $C_{sat} = C_0 e^{\frac{-\Delta H_{sol}}{kT}}$ Table 3.1 using a non-linear least squares regression.

Table 3.1. Parameters for water solubility in encapsulants

	406	806	TF4	TF8
$C_0(\frac{g}{cm^3})$	10±3.29	70.5 ±53.1	438±541	35.9±27.5
ΔH_{sol} (eV)	0.22±0.009	0.27±0.021	0.37±0.03	0.30±0.02

The result of a t-test with unequal variances showed no significant difference in the solubility between plain and UV blocking polymers for both EVA and POE encapsulants. As expected, the solubility of the EVA is higher than the POE because of the polar vinyl acetate groups that encourage water bonding within the polymer matrix. In POE, nonpolar hydrocarbon chains allow for water to move freely throughout the polymer matrix, resulting in a lower solubility. During water bath testing, it is worth noting that the POE encapsulants did yellow over time, and this discoloration was more apparent in the UV-blocking POE blocks than the plain blocks. Yellowing in these encapsulants was only observed in POE blocks that were exposed to 80° C or higher baths for extended periods of time. Since the EVA and POE samples were saturated in the same baths, produced acetic acid from the EVA samples over time could diffuse into the surrounding water, causing the POE to appear yellow.

3.2 Optical Calibration Using WaRD

The baseline-subtracted absorbance values for the H2O peak (1902 nm) and the CH2 peak (1730 nm) were extracted to calculate the WaRD ratio ($\frac{A_{H_2O}}{A_{CH_2}}$) for each condition. The WaRD ratio values were plotted against the expected saturated water content of the polymer as determined by

the solubility parameters for each polymer type. An ordinary least squares model was fit to the calibration curves and used to predict the linear relationship between the polymer solubility and optical water signal. For the backsheet modules, the optical signal includes both the backside polymer (806 and TF8) and the backsheet. Theoretically, the WaRD method should work on both EVA and POE encapsulants as demonstrated by Kumar et al [42]. Both encapsulants alone have discernible water peaks within the detection limit of the instrument and do not have overlapping absorption features in the regions of interest.

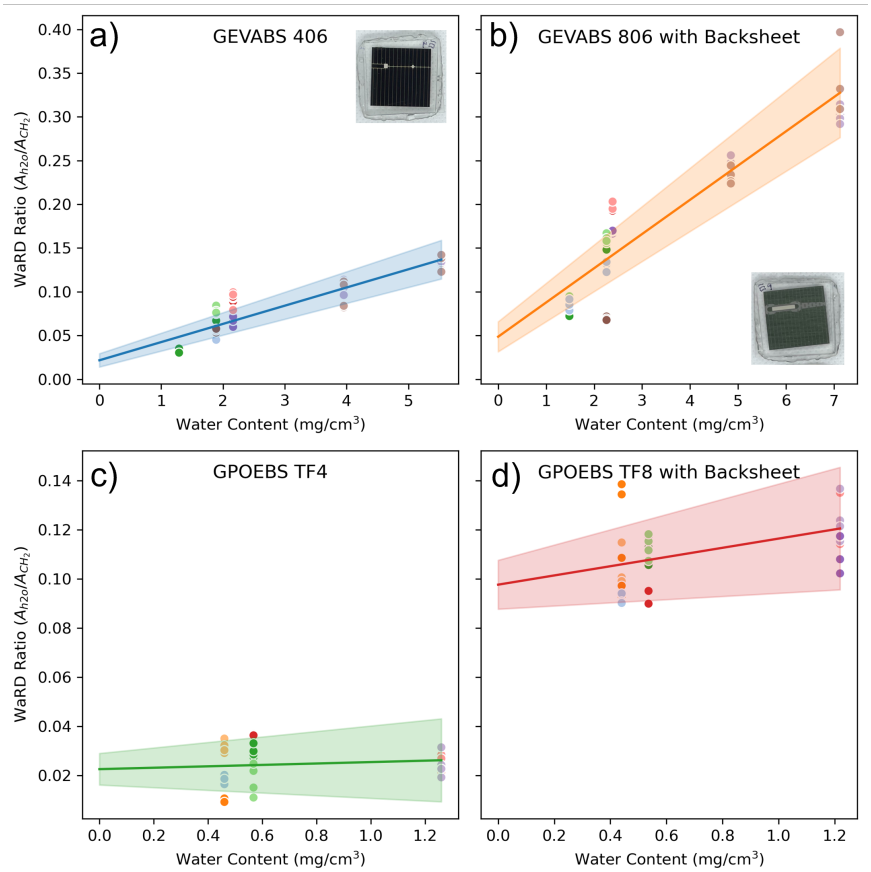

Figure 3.2. Glass-Backsheet WaRD Calibrations: The WaRD ratio signal plotted versus the expected water concentration of the polymer as calculated using the solubility for a) plain EVA, b) UV-blocking EVA, c) plain POE, d) UV-blocking POE. The expected water (x-axis) does not include the additional signal for the OH groups present in the backsheet (water and PET-core) in 806 and TF8. The insets show a frontside and backside of a bifacial module.

Polyolefins are more difficult to measure because of the lower water solubility (Figure 3.1), and this difficulty is amplified when measuring through a bifacial cell. The isola-

tion technique developed for the calibration of WaRD is necessary as bifacial cells are semi-transparent in this NIR region of interest. However, the metallization of these cells is designed to reduce reflectance and as a result the optical signal is not consistent along the length of the finger. Multiple measurements along different fingers at different y values were taken to average variations in signal across the cell. This method worked for the 406 and 806 polymers, but the POE encapsulants showed little to no distinct linear trend with wide spread in the calculated WaRD ratios. Furthermore, the addition of the backsheet interferes with the absorption features of interest, specifically at 1902 nm where the water combination mode is sensitive to the OH groups in the PET core of the backsheet material. As a result, the WaRD ratios taken from the backside of the modules are more difficult to isolate and thus are inflated, as seen by the 806 and TF8 curves. A component of the backside bifacial cell, possibly the silicon nitride passivation, is also optically active at 1700 nm, as seen in Figure 2.4b, or the larger "jumps" in reflectance on the backside could be a result of the more dotted pattern of the backside metal contacts. Determining the location of a backside finger is not as consistent, where the characteristic peaks of reflectivity are wider than expected for these fingers.

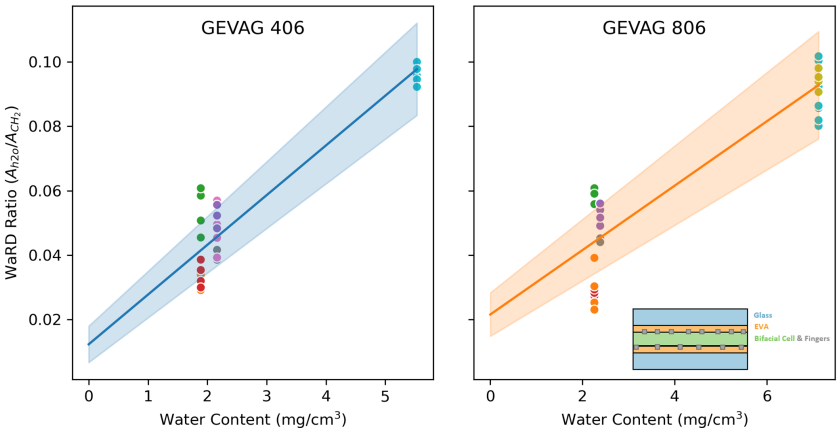

Figure 3.3. Glass-Glass WaRD Calibrations: The WaRD ratio signal plotted versus the expected water concentration of the polymer as calculated using the solubility for a) plain EVA, b) UV-blocking EVA. The x-axis is accurate because of the absence of the backsheet. The inset is schematic of a glass-glass configuration module.

The glass-glass calibration for the EVA shows that the calibration for the plain and

UV-blocking polymers are comparably similar. This calibration is more accurate for determining the isolated water concentration of the backside.

3.3 Model Validation of Water Out Diffusion in Bifacial Modules using FDM

We measured the 1700-2000 nm reflection along the width of a partially saturated GBS bifacial half cut cell module for 10 hours, with one full scan along the module per hour. The sample was measured on a heated stage at 85°C to prevent condensation and the laser setup was in ambient conditions. Figure 3.4a shows the change in water concentration along the module during the duration of the dry-out of the polymeric encapsulants (EVA). The water concentration in the sample decreases as a function of position and time. We expect the water concentration profile to be "bowl" shaped since the module was partially saturated initially. We do not expect a large decrease in the frontside polymer water content during the duration of the dry out because of the initial condition of the module and the length of the measurement. Given a half-cut cell with a minimum diffusion length of 39 mm, the expected time to reach 99% saturation is 15-20 days at 85°C. Symmetry between the top and bottom of glass-glass modules makes fitting these data simple, as water moves in unison on both sides. In glass-backsheet modules, we fit the front and back separately by assuming that, as the module begins drying from a water-saturated condition, the water content on the center of the front side (far from the module edges) remains constant until after the back side has completely dried out. The initial loss in water content at this point, therefore, represents the dry-out of the backside alone (Figure 3.4b). The backside EVA and backsheet have a combined thickness of 640 μm and were saturated at the beginning of the measurement. The backside isolated data was fit (Eq. 2.2) using the initial and boundary conditions (Eq. 2.3 and Eq. 2.4). The diffusivity for the backside polymer and backsheet was predicted to know the backside water content as a function of time. This quantity is subtracted from the total measured gradient to leave only the frontside isolated water content (Figure 3.4c).

Note that only the edges of the frontside water content dry out over the ten hours tested in Figure 3.4c owing to the large diffusion length for lateral out-diffusion in the module.

We developed a model based on using WaRD to non-invasively predict accurate diffusivities of polymers in bifacial modules. By using the finite difference method to solve the diffusion equation, the model is valid when the initial concentration of water is unknown in module, which is ideal for forward simulating weather data in real time. The flexibility of the model allows it to be more sensitive to multiple changing variables over time (e.g., temperature changing during measurement), such that diffusivity can be predicted per point, per time t, for all temperatures and relative humidities. The initial condition of the simulation mesh is interpolated from the first curve of the experimental data, so the first curve is not used for comparison during the non-linear ordinary least squares fit (Figure 3.4d). The simulated mesh is then padded with the boundary and initial conditions (Eq. 2.6 and Eq. 2.7) to closely match the real surroundings. As seen in Figure 3.4e, the encapsulant in the module extends beyond the area of the cell, where the shortest diffusion length for water is then the thickness of the EVA layers with the backsheet. At $t = 0$, the initial condition of the surrounding polymer is equivalent to the edge value of the experimental data, which is assumed to be saturated with the expected water concentration at 85°C, 85%RH because of the shorter diffusion length. Since it is expected that the water will diffuse out of the backside once it reaches the edge of the cell, the minimum amount of padding needed for the simulation is equal to the thickness of the encapsulants (total thickness is 640 μm, therefore 1 point is added to each side for a mesh with a step size of 500 μm). The mesh is again padded once more with a value to represent the fixed source Dirichlet boundary condition at the surface of the polymer layer (ambient temperature and relative humidity, 25°C 55% RH). Using these assumptions, we used the experimental data to validate the functionality of this model to predict the diffusivity of the front and backside polymers simultaneously in a bifacial cell.

Our complete model for simulating the behavior for the encapsulants also predicts the signal sensitivity, R_{GB}, between the frontside and backside (Eq. 2.10) and is useful for the application of measuring reflectance on bifacial modules or NIR-translucent solar cells. Since

the bifacial cell is semi-transparent in the NIR region of measurement, line scans across the cell will contain information from both sides of the module, and the amount of information will depend on the location of the fingers and their offsets. This sensitivity value is a measure of the fraction of backside signal collected when measuring from the frontside of the module. We predicted this value to be around 0.063 for this simulation and have consistently returned results near this value using other experimental data on bifacial mini modules. As seen from Eq. 2.10, this value is sensitive to the prediction of the initial backside concentration $C_{0,back}$ and will increase dramatically in certain local minima. However, these unreasonable values do not result in useful simulations and are not considered to be significant to this model.

3.3.1 Breathable Backsheet Compared to 806-only Diffusivity

Breathable backsheets are advertised to accelerate moisture ingress and egress in the backside encapsulant as compared to impermeable glass. These backsheets promote the out-diffusion of destructive by-products (acetic acid) as a result of the interaction of water with EVA encapsulants, reducing overall corrosion and yellowing [44]. They are shown here (Figure 3.4c) to not significantly limit the diffusivity of the backside polymer in these bifacial modules using the predicted values from the developed model (Eq. 2.2). For modeling the no backsheet module, the thickness of the backside encapsulant was changed to 300 μm for a single layer of EVA. The module was exposed to the same environmental conditions for the same duration of time, so the boundary and initial conditions were the same as for Figure 3.4. The padding values did not change because the resolution size of the mesh is larger than the new thickness of the backside encapsulant. It is also noted that by fitting a non-linear OLS to this experimental data, the predicted frontside polymer diffusivity was also consistent with the original experimental data on the GBS module ($D_{front} = 1.23\text{E-}5\ \frac{cm^2}{s}$ and $D_{front} = 1.77\text{E-}5\ \frac{cm^2}{s}$). It is worth noting the difference in water concentration values for both modules, where the module with a backsheet (Figure 3.4a) appears to have more water initially, even though the modules were exposed to the same damp heat condition for the same duration. The addition of the OH groups in the backsheet

material makes it easier to visualize and model the dry out of the backside encapsulants, especially compared to Figure 3.5b, where in the absence of a backsheet, modeling is still possible, but the backside is harder to see and fluctuation of the gradient at the center of the module is more apparent.

However, this brings up the question of whether we are observing the backside dry out, or only the backsheet dry out in our normal packaged module. The FDM model described in Eq. 2.10 depends on the uniform, visible translation of the water concentration profile to represent the backside dry out. Only the experimental data with a backsheet supports this model, whereas the experimental data without a backsheet is difficult to separate from the total concentration profile. When the average midpoint water concentration of Figure 3.5a is plotted over time, the data appears to be random with no explicit trend that is seemingly nonphysical. The same result is seen when measuring one point on the backside of this module over the same duration from the same initial condition, suggesting that the 300 μm EVA-only layer dries out faster than can be measured using the current WaRD setup. The addition of a layer of PET-core backsheet will rate-limit the diffusivity of the EVA layer, and the FDM modeling is unable to identify the rapid loss of water from a single layer of thin polymer. Therefore the diffusivity of the polymer block samples should be collected to pursue this question further.

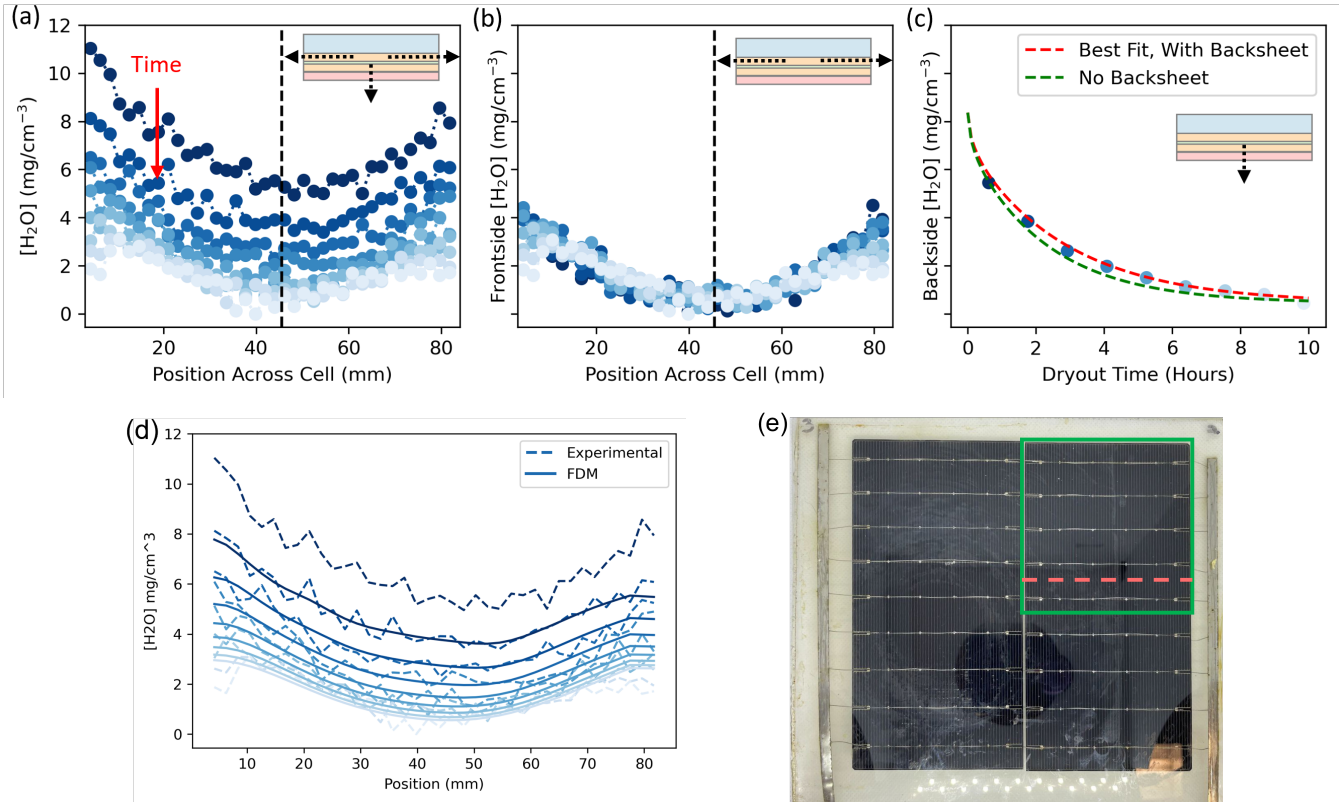

Figure 3.4. Experimental out-diffusion and application of FDM model: (a) Raw data of the water concentration across the profile of an 8x8" glass-EVA-backsheet module with a half-cut cell. Line scans were measured across the width of the cell (short dimension) as shown in (e). Assuming symmetry in the module, only one quarter of the module was measured. The module was exposed to damp heat conditions (85°C, 85% RH) in an environmental chamber for approximately 6 days prior to measuring. The module was measured on a heated stage at 85C to prevent condensation. The out-diffusion of the module was measured for 10 hours (from dark blue to light blue in the figure). The inset on the figure is a diagram representing the out-diffusion paths of water on both sides of the module (lateral frontside and uniform backside) over the 10 hour dry out period. (b) The resultant isolated frontside water concentration in the profile calculated by subtracting the data from (a) by the fitted backside water in (c). The inset diagram shows that the data represents the lateral diffusion of water from the center of the polymer (no flux assumption at the line of symmetry) to the edges of the cell. The diffusion length is half the width of the cell. (c) The average midpoint water concentration of each line scan plotted over the dry out time representing the backside isolated water out-diffusion in the module. The inset diagram represents 1D uniform out-diffusion of water from the encapsulant through the backsheet to the surroundings. The backside-isolated diffusivity was measured on sister modules with and without a backsheet. (d) The result of the model prediction of the water concentration profile of a glass-backsheet EVA module as compared to the experimental data from (a). Figures (a), (b), and (c) show the process of isolation of the water concentrations of the front and backsides of the GBS module to create the model. (e) The 8x8" glass-EVA-backsheet half cut cell module that was measured along the red dashed line.

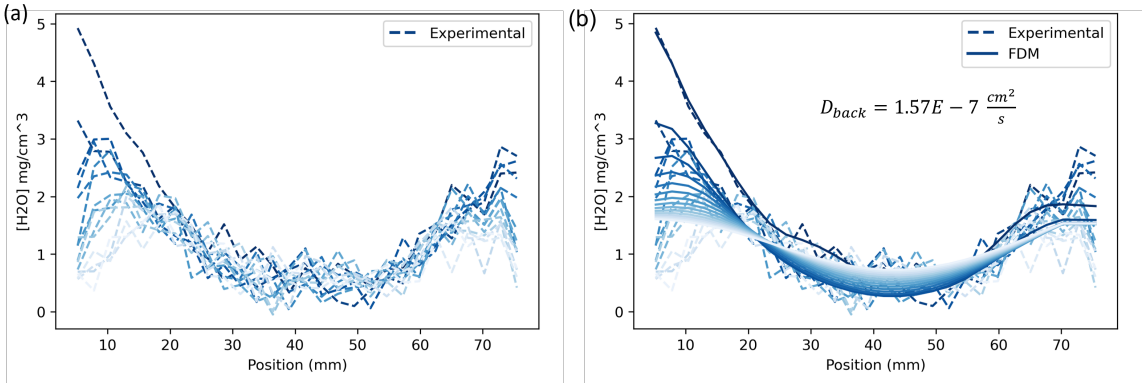

Figure 3.5. Diffusion of polymers with and without a backsheet: (a) Experimental data of the 14 hour dry out at 85°C of an 8x8" glass-no backsheet EVA half cut cell module. (b) The same experimental data and the model prediction of the water concentration profile. The sample was saturated to the same initial conditions as the sample in Figure 3.4 before being measured in the same process. The comparison of the diffusivities of both configurations are shown in Figure 3.4c. The diffusivity of the backside polymer (in this case, polymer 806) is similar to the observed diffusivity with a layer of backsheet.

3.4 Real Time Simulation of Bifacial Modules as a Function of Local Climate, Cell Cut Size, Module Architecture, and Initial Conditions

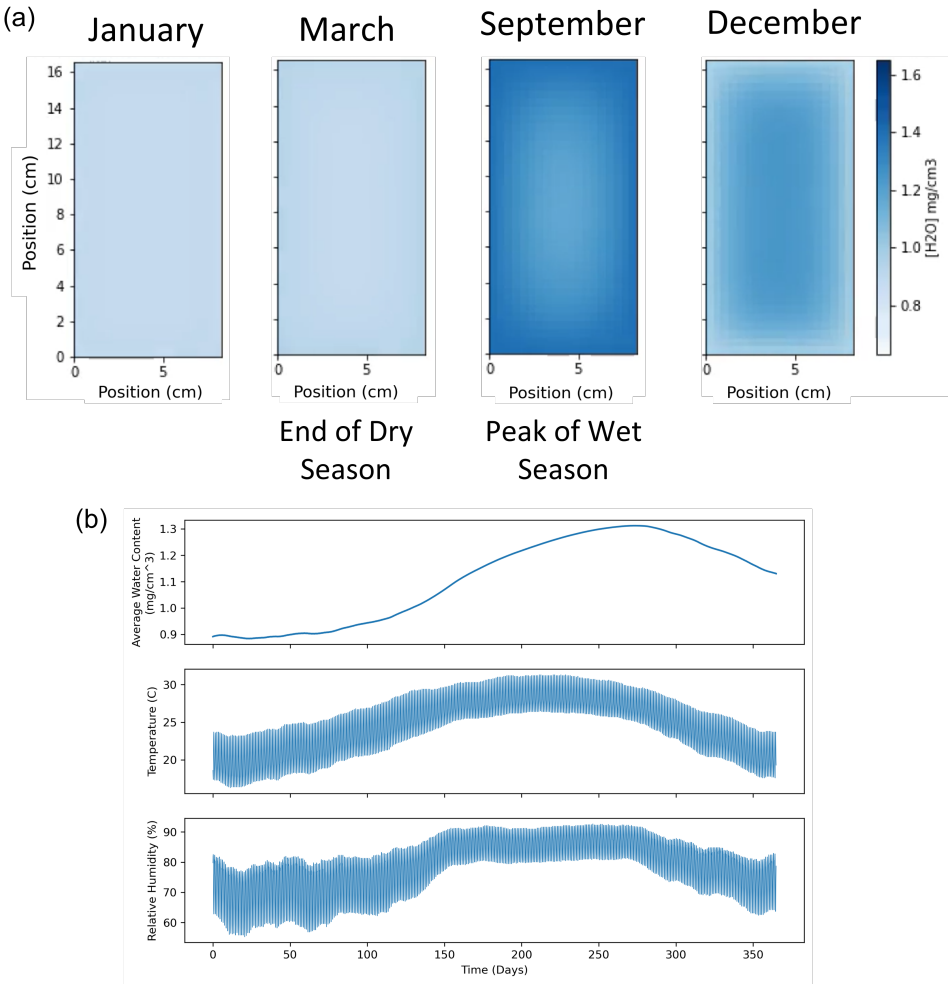

Figure 3.6. 2D simulation of a half cut cell "breathing" water in Miami, FL: (a) The 2D water concentration profile of the frontside of a GBS EVA half cut cell over 1 year using historical weather data. Four snapshots of the simulation are used to represent four condition extremes during the year given the historical data. b) The average water concentration within the frontside of the module at each time step with the temperature and relative humidity. Weather data retrieved from [48].

Here, we present the application of the validated model to simulate the 2D water concentration profile of a solar cell. Because of the flexibility of the FDM solution, diffusivity can be calculated per point per time t for any environmental condition given the calibration curve, and

then used to simulate the water breathing in the module. Figure 3.6a shows the change in the water concentration of the frontside EVA (406) in Miami, Florida at time $t = 0$ (January), where the module initialized with the equivalent water concentration of EVA 406 at 25 °C, 60% RH. The next profile is shown at the end of the dry season in March, where in this case, the initial condition of the module was close to the average temperature and relative humidity of Miami in the winter. The saturation of the module in March is misleading because of the influence of the initial condition of the module on the water behavior until the encapsulant equilibrates to the local climate conditions. The profile of the module in September is almost entirely saturated after the damp heat climate in the summer. Prolonged exposure to high heat, high humidity events causes water to accumulate within the module and accelerate various module degradation pathways. The water within the module is also prone to condensation, which is dependent on the module temperature and the dew point [49]. The final snapshot of the water profile in December shows how the drier conditions in the fall lead to water egress out of the module that will extend into the winter. We extend the use of this simulation further by exploring the effect of wafer size on water breathing.

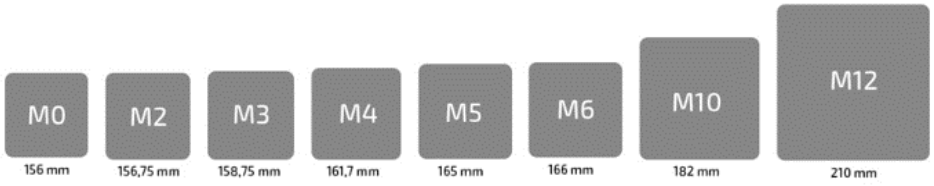

Figure 3.7. Evolution of silicon wafer size [50]

Increasing the wafer size improves the power generation capacity of the overall module and the LCOE without driving up costs [51], [52]. From the perspective of degradation, larger wafer sizes can be susceptible to excessive water pooling due to their longer diffusion lengths with an impermeable glass layer. However, the longer diffusion length could also serve as an advantage because it takes longer for water to reach the center of the cell. Figure 3.8 shows that the highest average water concentration in the M12 wafer size is lower, even during the intense Miami summer. As water begins to quickly diffuse at the beginning of the wet season,

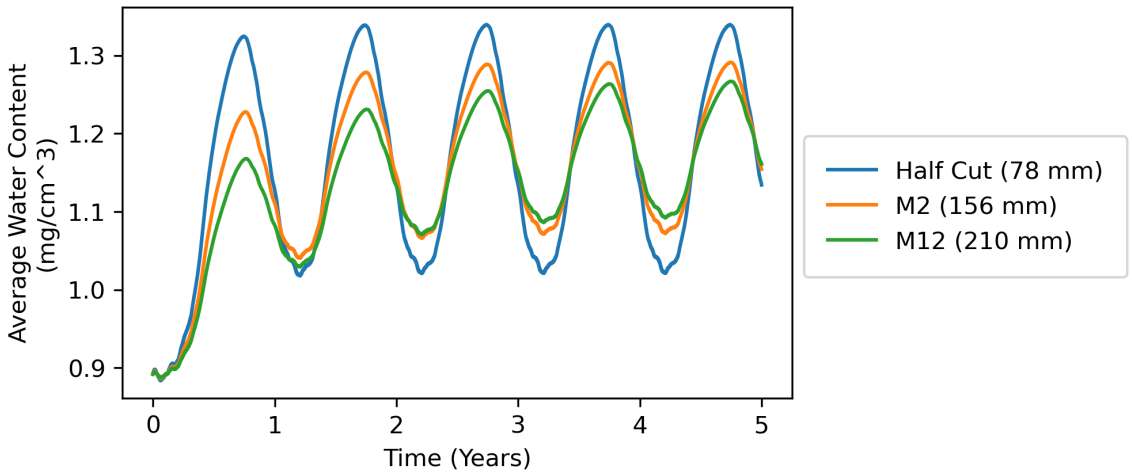

Figure 3.8. Average water concentration of GBS EVA half cell, M2 (full) cell, and M12 cell in Miami over 5 years

the diffusion length is so large that the climate begins to dry before the water has a chance to reach the line of symmetry at the center of the module, thus avoiding extensive moisture buildup. However, this behavior is vulnerable to the initial condition of the module. The water concentration profile snapshots are presented in Figure D.1.

Compared to Miami, we expect modules in solar-viable low moisture climates such as Phoenix, Arizona to endure less moisture induced degradation. The simulation of the water concentration profile over time for a module in Phoenix highlights the impact of the initial condition of the module. A module laminated at 25 °C, 60% RH is already in equilibrium with the local climate in Miami, but Figure 3.9 shows that a saturated module at that condition would not naturally occur when exposed to the climate in AZ for 1 year. The effect of the initial condition persists throughout the year for the M2 (full) cell module, where the center of the module is considerably more saturated in December than the half cut cell, reversed from the behavior exhibited by the same sized modules in Miami (Figure 3.8).

Lastly, we utilize this mapping simulation to monitor the oscillatory behavior of the average water concentration over an extended period of time, in this case 5 years (Figure 3.10). To improve the accuracy of the simulation, we would apply the same FDM to the backside layer

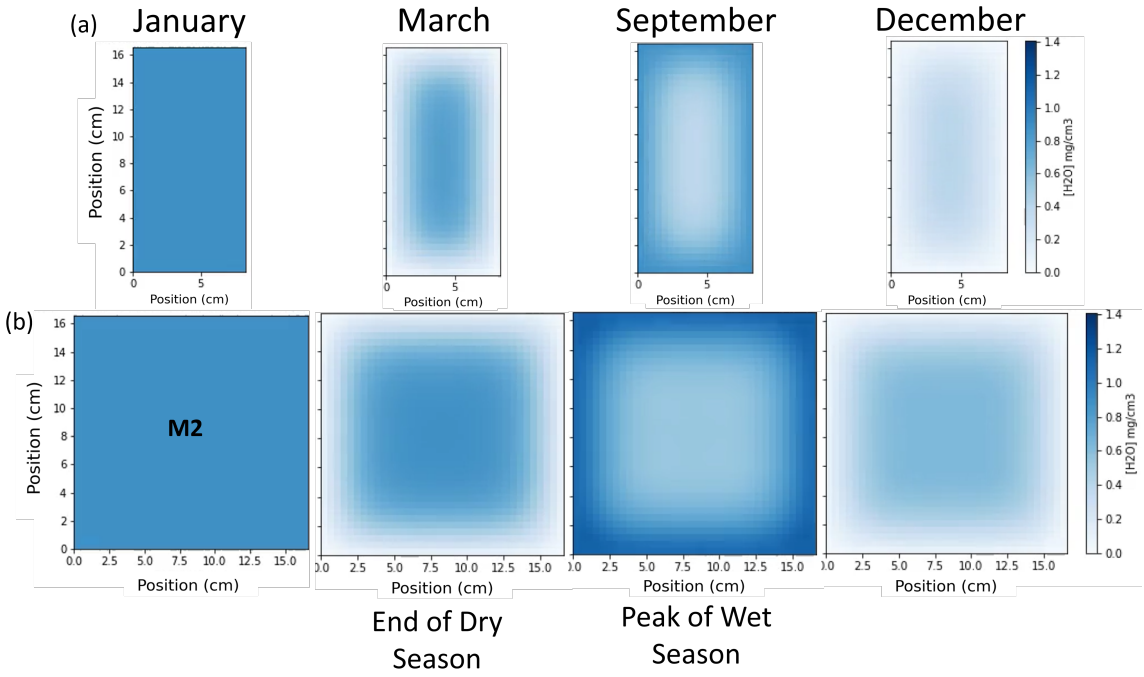

Figure 3.9. 2D simulation of GBS frontside EVA half cut and M2 sized wafers in Phoenix, AZ over 1 year

encapsulant of a GBS module during the life cycle to isolate how water is behaving on both sides. This way we can compare the water accumulation behavior in GBS and GG to predict the best module configuration for a specific type of climate. Additionally, we could estimate module temperature as outlined by Kempe [49] to flag when condensation events arise, especially in the larger sized GG modules where we expect most of these to occur after a day in a hot and humid climate, followed by a colder, dewey morning.

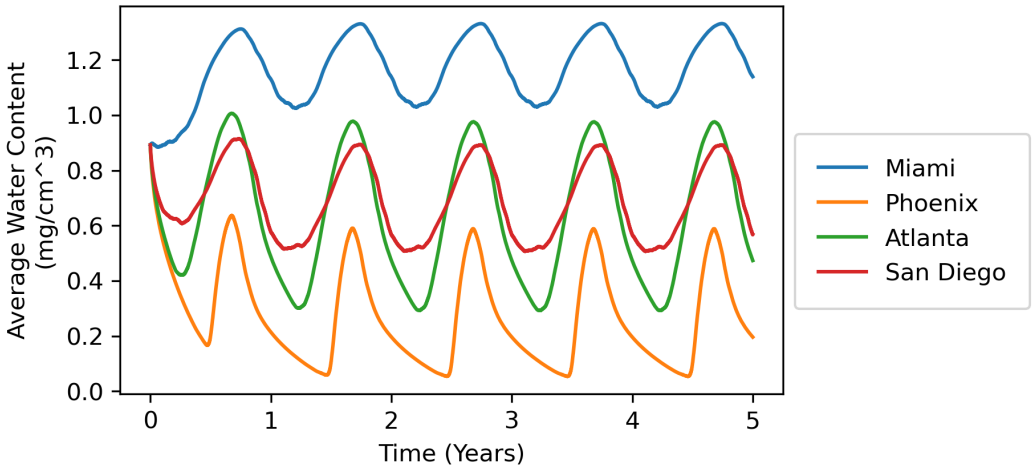

Figure 3.10. Average water concentration of GBS EVA half cell modules in Miami, Phoenix, Atlanta, and San Diego over 5 years

Chapter 4

Conclusion

This study explores the application of using water reflectometry detection to quantify water behavior for industry relevant alternatives to encapsulants and module configurations for bifacial silicon photovoltaic modules. We present the parameters necessary to model moisture transport in contemporary polyolefin and ethylene vinyl acetate encapsulating polymers. UV-blocking additives are shown to have a negligible effect on the solubility of water in these encapsulants. By measuring at the bandgap of silicon and on the metallizations, we demonstrate a reproducible method for isolating the reflectance signal from both sides of a bifacial PERC cell. Using this technique and WaRD, we can calibrate and measure the movement of water in mini modules and large half cut modules with EVA polymers. The application of the WaRD method on POE polymers in bifacial cells requires more careful measurement and further work to achieve. With a calibration and appropriate water parameters, we constructed a model for moisture dynamics in bifacial PV modules validated by our experimental data in accelerated testing conditions. Finally, we utilize the model to simulate the behavior of moisture ingress to quantitatively identify the effect of climate and cell size on potential degradation in PV modules. Future work on this study could explore the application of WaRD on alternative polymers (ionomers) with a robust method for repeatably measuring on bifacial modules. Additionally, the framework of the simulation leaves room for improvements like using the relevant diffusivity of the polymers used in this study to more accurately predict the behavior of the modules calibrated.

Even further, the addition of the module temperature will change the local diffusivity of the polymer, which will affect the observed behavior. Finally, the 2D FDM can be adapted to model the diffusion for the thinner backside encapsulant layer, allowing for the simultaneous simulation of both the front and backside polymers in different configurations.

Appendix A

Calibration

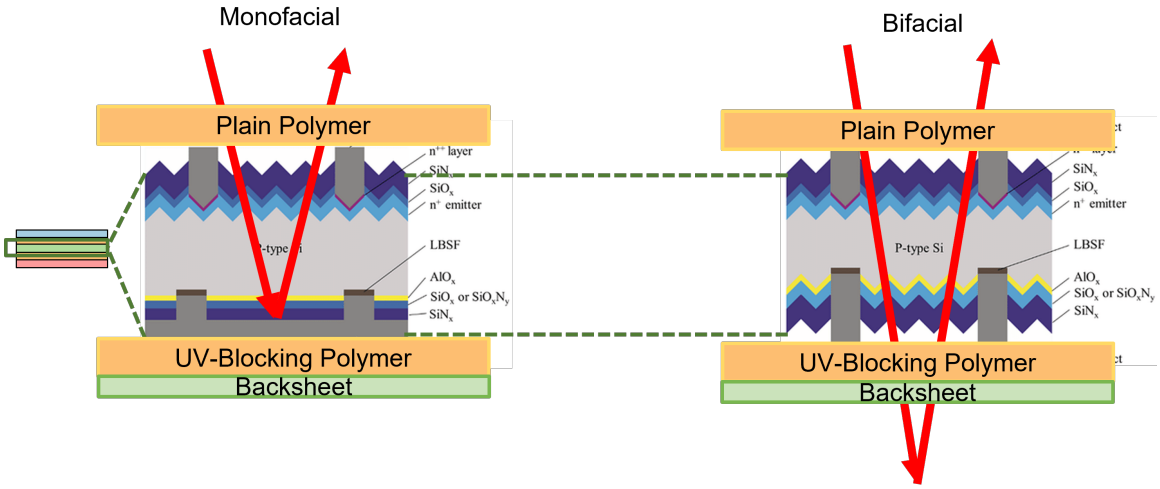

Figure A.1. Schematic of the WaRD calibration method on an Al-BSF silicon cell (original) and the use of the method on a bifacial PERC cell. Both types of cells are transmissive in the region of the SWIR light used to quantify the water signal, but the monofacial cell has a back contact that only allows for the frontside water signal to return during the measurement. The bifacial module does not have the same back contact layer, so the SWIR light will pass through the entirety of the module until it reflects off the surrounding environment (in this case, the stage holder for the sample instrument). Cell images from [53].

Appendix B

Isolation

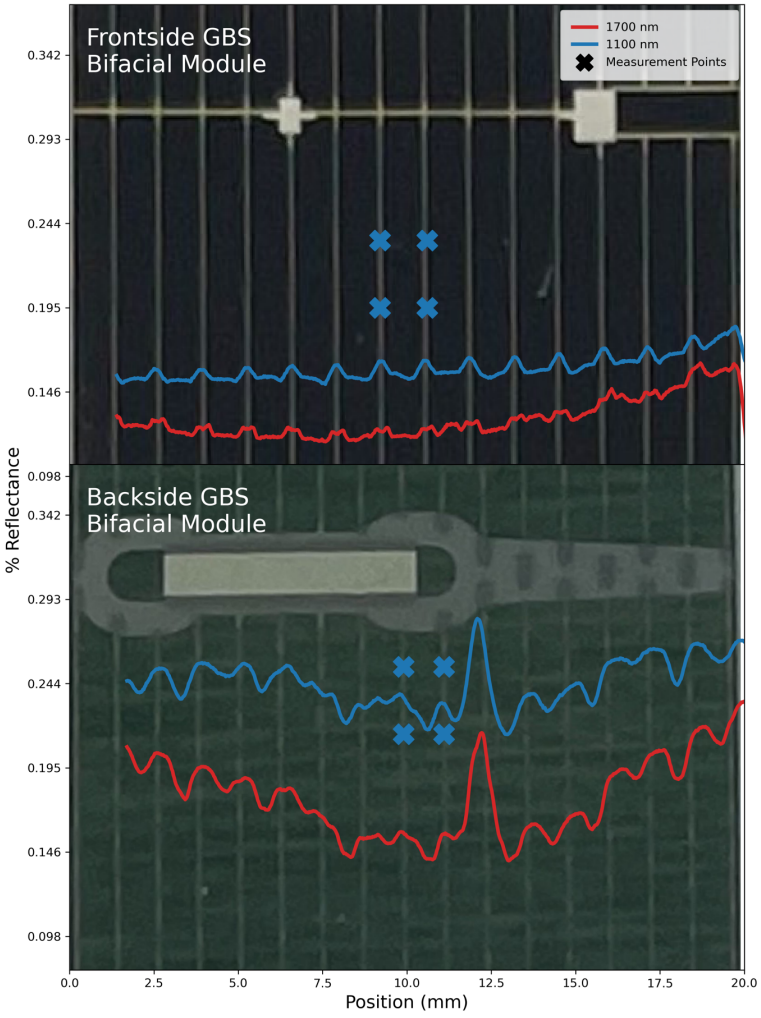

Figure B.1. Line scans at 1100 and 1700 nm along the width of a GBS EVA mini module with markers showing measurement points along fingers

Appendix C

Diffusion Pathways

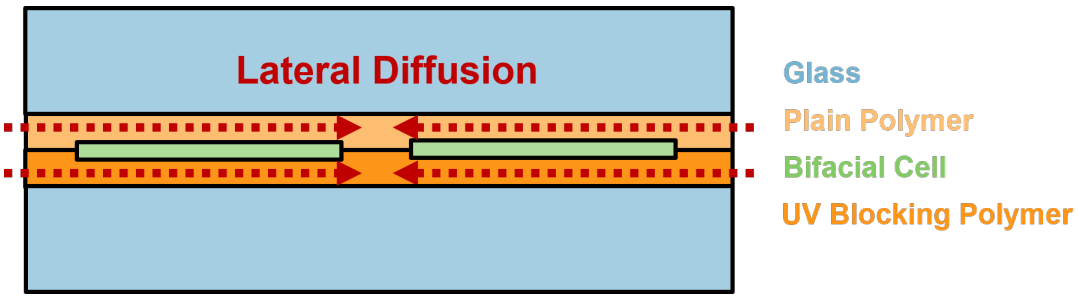

Figure C.1. Schematic of the lateral diffusion pathway within a fully encapsulated glass-glass module with multiple cells

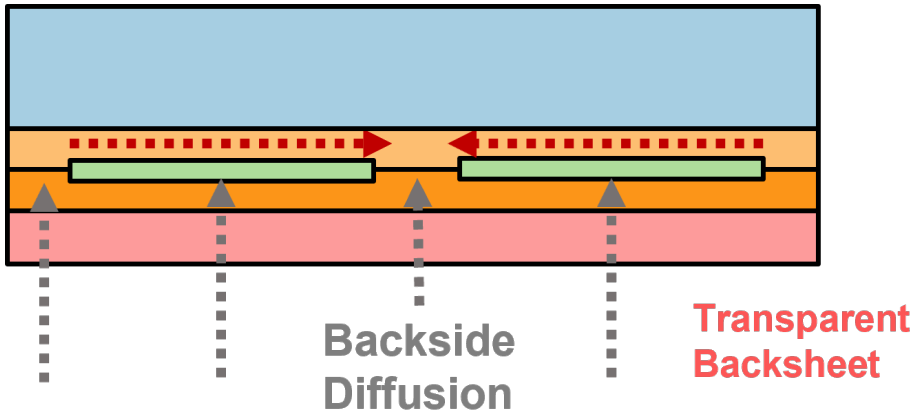

Figure C.2. Schematic of the lateral and backside diffusion present in a fully encapsulated glass-backsheet module with multiple cells

Appendix D

Simulations

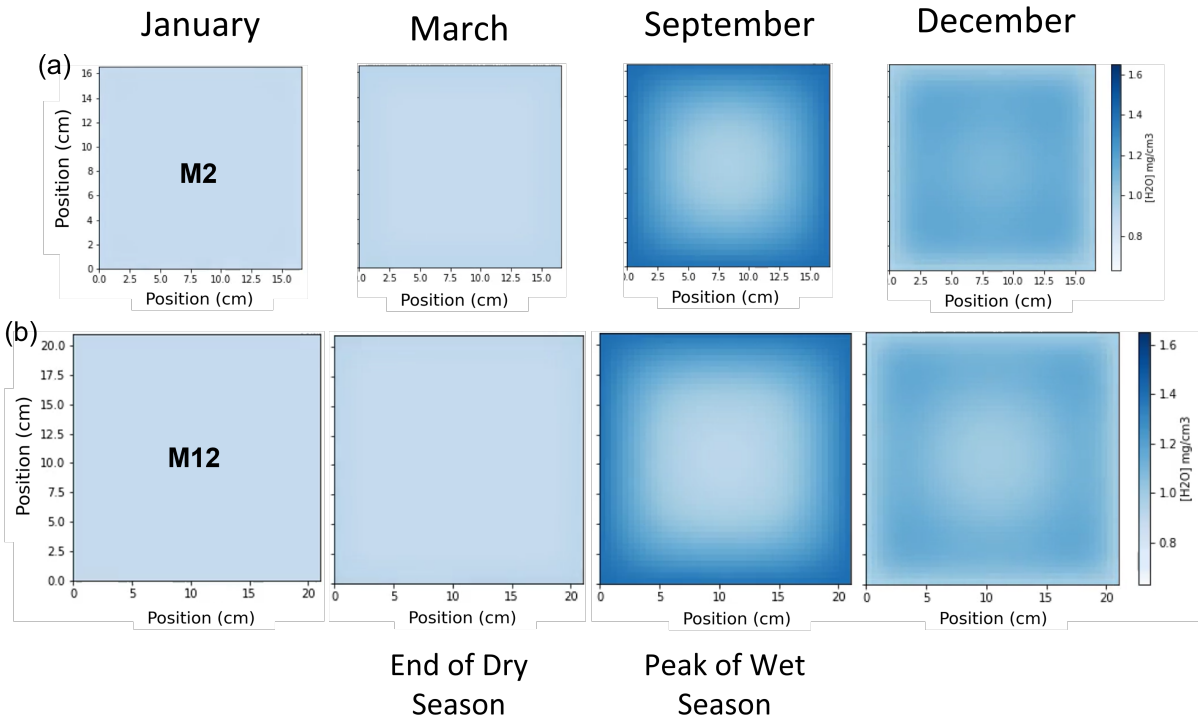

Figure D.1. 2D simulation of GBS frontside EVA M2 and M12 sized wafers in Miami over 1 year

Chapters 1-4, in full, are currently being prepared for submission for publication of the material. Sidawi, Tala; Kumar, Rishi E.; Slauch, Ian; Meier, Rico; Bertoni, Mariana I.; Fenning, David P. The thesis author was the primary investigator and author of this material.

Bibliography

[1] Max Roser Hannah Ritchie and Pablo Rosado. Energy. *Our World in Data*, 2020. https://ourworldindata.org/energy.

[2] John Asafu-Adjaye. The relationship between energy consumption, energy prices and economic growth: time series evidence from asian developing countries. *Energy economics*, 22(6):615–625, 2000.

[3] IEA. World energy outlook 2021. *World Energy Outlook*, 2021. https://www.iea.org/reports/world-energy-outlook-2021.

[4] David Feldman, Vignesh Ramasamy, Ran Fu, Ashwin Ramdas, Jal Desai, and Robert Margolis. Us solar photovoltaic system and energy storage cost benchmark: Q1 2020. Technical report, National Renewable Energy Lab.(NREL), Golden, CO (United States), 2021.

[5] BloombergNEF. Bloomberg new energy outlook finance. 2017. https://about.bnef.com/new-energy-outlook/.

[6] Nathan S Lewis, George Crabtree, AJ Nozik, MR Wasielewski, P Alivisatos, H Kung, J Tsao, E Chandler, W Walukiewicz, M Spitler, et al. Basic research needs for solar energy utilization. report of the basic energy sciences workshop on solar energy utilization, april 18-21, 2005. Technical report, DOESC (USDOE Office of Science (SC)), 2005.

[7] Thomas Surek. Crystal growth and materials research in photovoltaics: progress and challenges. *Journal of Crystal Growth*, 275(1-2):292–304, 2005.

[8] Aesha Parimalbhai Patel, Archana Sinha, and Govindasamy Tamizhmani. Field-aged glass/backsheet and glass/glass pv modules: encapsulant degradation comparison. *IEEE Journal of Photovoltaics*, 10(2):607–615, 2019.

[9] Keita Arihara, Ryosuke Koyoshi, Yasuhiro Ishii, Masaru Kadowaki, Atsushi Nakahara, Hitoshi Nishikawa, Taiki Takayama, Hiroyuki Nishimura, Kinichi Ogawa, Yasuo Chiba, and Atsushi Masuda. Reliability and long term durability of bifacial photovoltaic modules using transparent backsheet. volume 57. Japan Society of Applied Physics, 8 2018. doi:

10.7567/JJAP.57.08RG15.

[10] Sara Wolf. What are bifacial solar panels, Dec 2019. URL https://www.paradisesolarenergy.com/blog/what-are-bifacial-solar-panels.

[11] Max Mittag, Alex Grünzweig, Martin Wiese, Nabil Mahmoud, Alexandra Schmid, and Martin Heinrich. Analysis of backsheet and rear cover reflection gains for bifacial solar cells. In *33rd European PV Solar Energy Conference and Exhibition*, volume 2017, 2017.

[12] A Cuevas, A Luque, J Eguren, and J Del Alamot. 50 per cent more output power from an albedo-collecting flat panel using bifacial solar cells, 1982.

[13] Thorsten Dullweber, Christopher Kranz, Robby Peibst, Ulrike Baumann, Helge Hannebauer, Alexander Fülle, Stefan Steckemetz, Torsten Weber, Martin Kutzer, Matthias Müller, et al. Perc+: industrial perc solar cells with rear al grid enabling bifaciality and reduced al paste consumption. *Progress in Photovoltaics: Research and Applications*, 24(12):1487–1498, 2016.

[14] Andreas Hubner, A Aberle, and Rudolf Hezel. Temperature behavior of monofacial and bifacial silicon solar cells. In *Conference Record of the Twenty Sixth IEEE Photovoltaic Specialists Conference-1997*, pages 223–226. IEEE, 1997.

[15] R Hezel. A novel high-efficiency rear-contact solar cell with bifacial sensitivity, 2009. URL https://doi.org/10.1007/978-3-540-79359-5_6.

[16] Dupont and jinkosolar join forces to launch swan module with transparent backsheet, Dec 2018. URL https://www.dupont.com/news/dupont-photovoltaic-solutions-and-jinkosolar-join-forces-to-launch-high-efficiency-bifacial-module.html.

[17] Joshua Morse, Michael Thuis, Derek Holsapple, Ryan Willis, Michael D Kempe, and David C Miller. Degradation in photovoltaic encapsulant transmittance: Results of the second pvqat tg5 artificial weathering study. *Progress in Photovoltaics: Research and Applications*, 2022.

[18] Alan J. Curran, Dylan Colvin, Nafis Iqbal, Kris O. Davis, Thomas Moran, Bryan D. Huey, Brent Brownell, Ben Yu, Jean-Nicolas Jaubert, Jennifer L. Braid, Laura S. Bruckman, and Roger H. French. Degradation of perc and al-bsf cells with uv cutoff and white variations of eva and poe encapsulant. In *2021 IEEE 48th Photovoltaic Specialists Conference (PVSC)*, pages 1510–1516, 2021. doi: 10.1109/PVSC43889.2021.9519110.

[19] Sagarika Kumar, Hebatalla Alhamadani, Shaikha Hassan, Ahmad Alheloo, Hamed Hanifi, Jim Joseph John, Gerhard Mathiak, and Vivian Alberts. Comparative investigation and analysis of encapsulant degradation and glass abrasion in desert exposed photovoltaic

modules. In *2021 IEEE 48th Photovoltaic Specialists Conference (PVSC)*, pages 0793–0798. IEEE, 2021.

[20] Vijay Devabhaktuni, Mansoor Alam, Soma Shekara Sreenadh Reddy Depuru, Robert C Green II, Douglas Nims, and Craig Near. Solar energy: Trends and enabling technologies. *Renewable and Sustainable Energy Reviews*, 19:555–564, 2013.

[21] SS Chandel, M Nagaraju Naik, Vikrant Sharma, and Rahul Chandel. Degradation analysis of 28 year field exposed mono-c-si photovoltaic modules of a direct coupled solar water pumping system in western himalayan region of india. *Renewable Energy*, 78:193–202, 2015.

[22] Chris Deline, Nick DiOrio, Dirk Jordan, and Fatima Toor. Progress & frontiers in pv performance. Technical report, National Renewable Energy Lab.(NREL), Golden, CO (United States), 2016.

[23] Michael D Kempe, Arrelaine A Dameron, and Matthew O Reese. Evaluation of moisture ingress from the perimeter of photovoltaic modules. *Progress in Photovoltaics: Research and Applications*, 22(11):1159–1171, 2014.

[24] Philip Hülsmann and Karl-Anders Weiss. Simulation of water ingress into pv-modules: Iec-testing versus outdoor exposure. *Solar Energy*, 115:347–353, 2015.

[25] John H. Wohlgemuth and Sarah Kurtz. Using accelerated testing to predict module reliability. In *2011 37th IEEE Photovoltaic Specialists Conference*, pages 003601–003605, 2011. doi: 10.1109/PVSC.2011.6185927.

[26] Cher Ming Tan, Boon Khai Eric Chen, and Kok Peng Toh. Humidity study of a-si pv cell. *Microelectronics Reliability*, 50(9-11):1871–1874, 2010.

[27] Shan Jiang, Kemin Wang, Hongwen Zhang, Yonghong Ding, and Qiang Yu. Encapsulation of pv modules using ethylene vinyl acetate copolymer as the encapsulant. *Macromolecular Reaction Engineering*, 9(5):522–529, 2015.

[28] Abdérafi Charki, Rémi Laronde, and David Bigaud. Accelerated degradation testing of a photovoltaic module. *Journal of Photonics for Energy*, 3(1):033099, 2013.

[29] GR Mon, L Wen, RG Ross, and D Adent. Effects of temperature and moisture on module leakage currents. In *18th IEEE PVSC*, pages 1179–1185, 1985.

[30] Michele Cândida Carvalho de Oliveira, Antônia Sonia Alves Diniz Cardoso, Marcelo Machado Viana, and Vanessa de Freitas Cunha Lins. The causes and effects of degradation of encapsulant ethylene vinyl acetate copolymer (eva) in crystalline silicon photovoltaic modules: A review. *Renewable and Sustainable Energy Reviews*, 81:

2299–2317, 2018.

[31] Michael D. Kempe, Gary J. Jorgensen, Kent M. Terwilliger, Tom J. McMahon, Cheryl E. Kennedy, and Theodore T. Borek. Ethylene-vinyl acetate potential problems for photovoltaic packaging. volume 2, pages 2160–2163. IEEE Computer Society, 2006. ISBN 1424400163. doi: 10.1109/WCPEC.2006.279933.

[32] T. Grossetête, A. Rivaton, J.L. Gardette, C.E. Hoyle, M. Ziemer, D.R. Fagerburg, and H. Clauberg. Photochemical degradation of poly(ethylene terephthalate)-modified copolymer. *Polymer*, 41(10):3541–3554, 2000. ISSN 0032-3861. doi: https://doi.org/10.1016/S0032-3861(99)00580-7. URL https://www.sciencedirect.com/science/article/pii/S0032386199005807.

[33] Sagarika Kumar, Roopmati Meena, and Rajesh Gupta. Imaging and micro-structural characterization of moisture induced degradation in crystalline silicon photovoltaic modules. *Solar Energy*, 194:903–912, 2019. ISSN 0038-092X. doi: https://doi.org/10.1016/j.solener.2019.11.037. URL https://www.sciencedirect.com/science/article/pii/S0038092X19311351.

[34] Ju-Hee Kim, Jongsung Park, Donghwan Kim, and Nochang Park. Study on mitigation method of solder corrosion for crystalline silicon photovoltaic modules. *International Journal of Photoenergy*, 2014, 2014.

[35] Oscar Kwame Segbefia, Anne Gerd Imenes, and Tor Oskar Sætre. Moisture ingress in photovoltaic modules: A review. *Solar Energy*, 224:889–906, 2021.

[36] International Electrotechnical Commission et al. Thin film terrestrial photovoltaic (pv) modules—design qualification and type approval. *IEC International Standard, Geneva, Switzerland, Tech. Rep*, 61646, 2008.

[37] Jane Kapur, Kristof Proost, and C Anthony Smith. Determination of moisture ingress through various encapsulants in glass/glass laminates. In *2009 34th IEEE Photovoltaic Specialists Conference (PVSC)*, pages 001210–001214. IEEE, 2009.

[38] Johannes Hepp, Andreas Vetter, Stefan Langner, Michael Woiton, Gordana Jovicic, Klaus Burlafinger, Jens A Hauch, Christian Camus, Hans-Joachim Egelhaaf, and Christoph J Brabec. Infrared absorption imaging of water ingress into the encapsulation of (opto-) electronic devices. *IEEE Journal of Photovoltaics*, 9(1):252–258, 2018.

[39] C Peike, T Kaltenbach, K-A Weiß, and M Koehl. Non-destructive degradation analysis of encapsulants in pv modules by raman spectroscopy. *Solar Energy Materials and Solar Cells*, 95(7):1686–1693, 2011.

[40] Joseph A Curcio and Charles C Petty. The near infrared absorption spectrum of liquid water. *JOSA*, 41(5):302–304, 1951.

[41] GE Walrafen and Elijah Pugh. Raman combinations and stretching overtones from water, heavy water, and nacl in water at shifts to ca. 7000 cm- 1. *Journal of Solution Chemistry*, 33(1):81–97, 2004.

[42] Rishi E. Kumar, Guillaume Von Gastrow, Joswin Leslie, Rico Meier, Mariana I. Bertoni, and David P. Fenning. Quantitative determination of moisture content in solar modules by short-wave infrared reflectometry. *IEEE Journal of Photovoltaics*, 9:1748–1753, 11 2019. ISSN 21563403. doi: 10.1109/JPHOTOV.2019.2938108.

[43] Yanzhi Ren, Masahiko Shimoyama, Toshio Ninomiya, Kimihiro Matsukawa, Hiroshi Inoue, Isao Noda, and Yukihiro Ozaki. Two-dimensional near-infrared correlation spectroscopy studies on composition-dependent spectral variations in ethylene/vinyl acetate copolymers: assignments of bands due to ethylene units in amorphous, disordered, and orthorhombic crystalline phases. *Applied spectroscopy*, 53(8):919–926, 1999.

[44] G. J. Jorgensen, K. M. Terwilliger, J. A. DelCueto, S. H. Glick, M. D. Kempe, J. W. Pankow, F. J. Pern, and T. J. McMahon. Moisture transport, adhesion, and corrosion protection of pv module packaging materials. *Solar Energy Materials and Solar Cells*, 90:2739–2775, 10 2006. ISSN 09270248. doi: 10.1016/j.solmat.2006.04.003.

[45] Stephen W Hughes. Physics education, 2005. URL www.iop.org/journals/physed.

[46] M D Kempe and Michael D Kempe. Control of moisture ingress into photovoltaic modules, 2005. URL http://www.osti.gov/bridgeonlineordering:http://www.ntis.gov/ordering.htm.

[47] Luciano Rezzolla. Numerical methods for the solution of partial differential equations, 2020.

[48] National centers for environmental information. URL https://www.ncei.noaa.gov/.

[49] Michael D Kempe. Modeling of rates of moisture ingress into photovoltaic modules. *Solar Energy Materials and Solar Cells*, 90(16):2720–2738, 2006.

[50] Krannich Solar GmbH und Co.KG. Trends in pv cells and modules – module sizes and wafer sizes in transition - solar blog - krannich global solar distribution (en), May 2021. URL https://blog.krannich-solar.com/en/solarblog/post/trends-in-pv-cells-and-modules-module-sizes-and-wafer-sizes-in-transition.html.

[51] Radovan Kopecek and Joris Libal. Bifacial photovoltaics 2021: Status, opportunities and challenges. *Energies*, 14(8):2076, 2021.

[52] Vincent Shaw. Shifting to a larger solar wafer format: The rise of m6, Jan 2020. URL https://pv-magazine-usa.com/2020/01/28/the-weekend-read-the-rise-of-m6/.

[53] Tian Pu, Honglie Shen, Kuang Hong Neoh, Fei Ye, and Quntao Tang. Enhanced conversion efficiency of monocrystalline p-type passivated emitter and rear cells in commercial production line by improving rear side passivation. *Energy Technology*, 9(7):2001115, 2021.